Quarterly Progress Report No. 3

INVESTIGATION OF ELECTRON EMISSION CHARACTERISTICS OF LOW WORK FUNCTION SURFACES

by

L. W. Swanson
L. C. Crouser

Prepared for

Headquarters
National Aeronautics and Space Administration
Washington, D. C.

CONTRACT NASw-1082

Field Emission Corporation

McMinnville, Oregon

Requests for copies of this report should be referred to

National Aeronautics and Space Administration
Office of Scientific and Technical Information
Attention: AFSS-A
Washington, D.C. 20546

Quarterly Progress Report No. 3
For the Period
1 April 1965 to 30 June 1965

INVESTIGATION OF ELECTRON EMISSION CHARACTERISTICS OF LOW WORK FUNCTION SURFACES

by

L. W. Swanson
L. C. Crouser

Prepared for

Headquarters
National Aeronautics and Space Administration
Washington, D. C.

25 August 1965

CONTRACT NASw-1082

FIELD EMISSION CORPORATION
Melrose Avenue at Linke Street
McMinnville, Oregon 97218

TABLE OF CONTENTS

	Page
PURPOSE	1
ABSTRACT	2
PROGRESS TO DATE	3
TOTAL ENERGY DISTRIBUTION MEASUREMENTS	3
Experimental Techniques and Procedures	4
Theory	6
Total Energy Distribution	6
Results	12
Total Energy Distribution Measurements	12
Work Function Measurements at Elevated Temperatures	28
Discussion and Results	31
SUMMARY AND CONCLUSIONS	36
REFERENCES	38

LIST OF ILLUSTRATIONS

		Page
Figure 1.	Fowler-Nordheim plots as a function of temperature for two different planes of a tungsten emitter.	5
Figure 2.	Magnet current I required to deflect beam along the $[1\bar{1}0]$ zone of a $[00\bar{1}]$ oriented tungsten emitter.	7
Figure 3.	Recorder plots of the probe current I_c as a function of emitter bias voltage V_t at various temperatures.	13
Figure 4.	Theoretical total energy distribution plots based on the free electron model (equation 15) at various values of p.	15
Figure 5.	Experimental total energy distribution plots along the $[\bar{1}00]$ direction of a tungsten emitter as a function of p, where d = 0.174 ev and F = 4.08×10^7 v/cm.	16
Figure 6.	Experimental total energy distribution plots along the $[\bar{3}10]$ direction of a tungsten emitter as a function of p, where d = 0.137 ev and F = 3.06×10^7 v/cm.	17
Figure 7.	Experimental total energy distribution plots along the $[\bar{1}16]$ direction of a tungsten emitter as a function of p, where d = 0.138 ev and F = 3.04×10^7 v/cm.	18
Figure 8.	Experimental total energy distribution plots along the $[1\bar{1}2]$ direction of a tungsten emitter as a function of p, where d = 0.146 ev and F = 3.48×10^7 v/cm.	19
Figure 9.	Experimental total energy distribution plots along the $[\bar{1}11]$ direction of a tungsten emitter as a function of p, where d = 0.134 ev and F = 2.99×10^7 v/cm.	20
Figure 10.	Experimental normalized half-widths $d_{1/2}/d$ of the total energy distribution curves as a function of p. Solid line based on free-electron model (equation 15).	22
Figure 11.	Experimental normalized half-widths of the total energy distribution curves as a function of p. Solid line based on free-electron model (equation 15).	23
Figure 12.	Variation of relative peak height h of the experimental energy distribution curves as a function of p. Solid line based on free-electron model (equation 15).	24

Page

Figure 13. Variation of relative peak height h of the experimental energy distribution curves as a function of p. Solid line based on free-electron model (equation 15). 25

Figure 14. Experimentally observed variation of the position of the energy distribution peak relative to the Fermi level ϵ as a function of p. Solid line based on free-electron model (equation 15). 26

Figure 15. Experimentally observed variation of the position of the energy distribution peak relative to the Fermi level ϵ as a function of p. Solid line based on free-electron model (equation 15). 27

Figure 16. Variation of work function $\emptyset$ with temperature for the indicated planes as determined by Fowler-Nordheim plots analyzed according to equation 22. 30

Figure 17. Lomar model of the band structure of chromium (Ref. 9). The other group VI transition metals are probably similar. 32

Figure 18. First Brillouin zone of a body-centered cubic structure. Letters indicate directions of reciprocal lattice space used in Figure 17. 33

Figure 19. An extended section of the (100) plane in reciprocal lattice space. Each direction of hatching indicates the occupied states in a separate zone, and corresponds to the hatching of Figure 17. The dots indicate hole regions. 34

PURPOSE

The primary aims of this investigation are to obtain an improved fundamental understanding of (1) the phenomena governing the production of low work function surfaces, and (2) the factors affecting the quality and stability of electron emission characteristics. It is expected that the information generated from this investigation will be relevant to various kinds of electron emission (i.e., photo, thermionic and field emission), although the primary emphasis will be placed upon field emission. Accordingly, field emission techniques will be employed, at least initially, to obtain the objectives of this work.

The formation of low work function surfaces will be accomplished by; (1) adsorption of appropriate electro-positive adsorbates, (2) co-adsorption of appropriate electro-positive and electro-negative adsorbates, and (3) fabrication of emitters of low work function surfaces from various metalloid compounds. Various properties of these surfaces to be investigated in order to obtain a more fundamental understanding of them are the temperature dependency of the emission and work function, the various types of energy exchanges accompanying emission, the energy distribution of the field emitted electron, and various aspects of the surface kinetics of adsorbed layers such as binding energy, surface mobility and effect of external fields.

ABSTRACT

An investigation of the total energy distribution of field emitted electrons has been performed in the temperature range 77 - 900°K for five different crystallographic directions of a tungsten field emitter. The results obtained generally confirmed the contemporary field emission theory throughout the range of temperatures investigated. A theoretical discussion of the total energy distribution of field emitted electrons reveals that band structure effects, due to discrepancies from the free electron model generally assumed by contemporary field emission theory, are observed only in crystallographic directions exhibiting a Fermi surface of high radius of curvature. A review of existing solid state measurements of the band structure of tungsten indicates the possibility of significant anisotropies in the Fermi surface along the (100) direction. These expectations are reinforced by the anomalous shoulder on the total energy distributions about .35 ev below the Fermi level along the (100) directions.

Fowler-Nordheim plots as a function of temperature on several major planes of a tungsten emitter were analyzed to give the temperature dependence of the local work function. Over the temperature range 77 - 700°K both positive and negative temperature coefficients of the work function were observed depending on the particular crystallographic plane. For example, temperature coefficients on the (310), (112) and (100) planes were -3.2, -14.3 and -10.9 x 10^{-5} ev/deg respectively, whereas values of 5.0 and 3.5 x 10^{-5} ev/deg were observed on the (116) and (111) planes.

Author

PROGRESS TO DATE

Progress is being made in four general areas of investigation of low work function surfaces obtained by electro-positive metallic adsorption on tungsten and co-adsorption. They are: (1) emission heating; (2) energy distribution; (3) surface kinetics; (4) work function change on single crystallographic planes. The investigation of the preceding phenomena each involves different tube embodiments which have been construction and are currently being used to obtain results. Prior to the commencement of this investigation preliminary results were obtained on various aspects of work function change due to cesium adsorption and cesium-oxygen co-adsorption on tungsten. Some of these results, which have been reported elsewhere[1], have been analyzed in a previous report[2].

Measurements of the energy exchange accompanying field emission on clean and zirconium-coated tungsten emitters have been completed and show striking deviations from theory. Although the general features of the existing theory of "Nottingham" emission heating and cooling were confirmed, certain discrepancies were noted between experiment and theory in regard to the amount of energy exchanged per electron and the value of the temperature boundary which separates emission heating and cooling. The discrepancies between the inversion temperatures determined by measurements of the total energy distribution and the Nottingham effect may be due to a preponderance of conduction by holes below the Fermi level at elevated temperatures. It is further suggested that the free-electron model of tungsten is not adequate for describing the Nottingham effect and band structure effects must be taken into consideration.

In order to shed further light on the bulk electronic properties of tungsten, a detailed investigation of the total energy distribution of field emitted electrons has been completed and described in the current report. It will be shown that, due to the insensitivity of field emitted electrons to the specific band structure of a metal, the free-electron theory is reasonably applicable to describing field emission phenomena and total energy distribution in spite of the fact that the bulk electronic properties of tungsten may show marked deviation from free electron theory.

TOTAL ENERGY DISTRIBUTION MEASUREMENTS

The average energy of the emitted electrons and the inversion temperature obtained from investigations of the Nottingham effect can be checked by comparison with the corresponding experimentally determined total energy distributions. A preliminary investigation of the total energy distribution of field emitted electrons from clean tungsten over the temperature range 77 - 1059°K has been reported earlier[2]. These results, which showed reasonable agreement with contemporary field emission theory, have been

extended to the following crystallographic directions: [100], [130], [116], [112], and [111].

EXPERIMENTAL TECHNIQUES AND PROCEDURES

The description of the energy analyzer tube and its mode of operation were described in an earlier report[2]. Briefly, the tube was designed in such a way that electrons passing through a lens system were focused near the center of a hemispherical collector. The electrode system of the analyzer consisted of an anode, a lens electrode and a Faraday cage surrounding the hemispherical collector. The Faraday cage electrode was operated near ground potential and acted as a shielding electrode for the hemispherical collector (also operating near ground potential) and accordingly reduced the effect of undersirable reflection inherent in most retarding potential analyzers.

In practice, the anode potential V_A is constant and the focal length adjusted by varying the potential of the lens electrode V_L. The total energy distribution curves were taken for fixed values of V_L and V_A by varying the cathode potential between -4.0 and -5.5 v, depending upon the work function of the collector. The ratio V_L/V_A is a critical quantity and for this particular lens system best results were obtained with $V_L/V_A = 0.0035$.

A small external electromagnet and internal concentrator were used to deflect the beam in order to position the emission from the desired crystallographic plane on the aperture of the anode electrode. With this arrangement the tube could be used to measure both energy distributions and work functions from different crystallographic planes. The I-V data for work function measurements were obtained with the tip at -8 volts and a constant ratio of V_L/V_A in order that the electron trajectories through the lens would be constant over the voltage range. During the I-V measurements with magnetic deflection, compensation of the magnetic current must be performed in order to maintain a constant position of the desired crystallographic plane on the aperture over the voltage range. Analysis of the I-V data in the form of a Fowler-Nordheim plot for two different crystallographic planes of tungsten as a function of temperature are given in Figure 1. Work functions and energy distribution and measurements were taken along a particular zone line at positions where the current went through a maximum or a minimum as a function of the deflection. This allowed precise positioning of the desired plan on the aperture of the anode over the voltage range covered by the Fowler-Nordheim plot. Further analysis of this data will be given in a later section.

The resolution of this analyzer tube was estimated at 10 mv by Dr. Van Oostrom[3]. Normally resolution is ascertained by comparison of the experimental and theoretical curves. Unless rigorous analysis of all

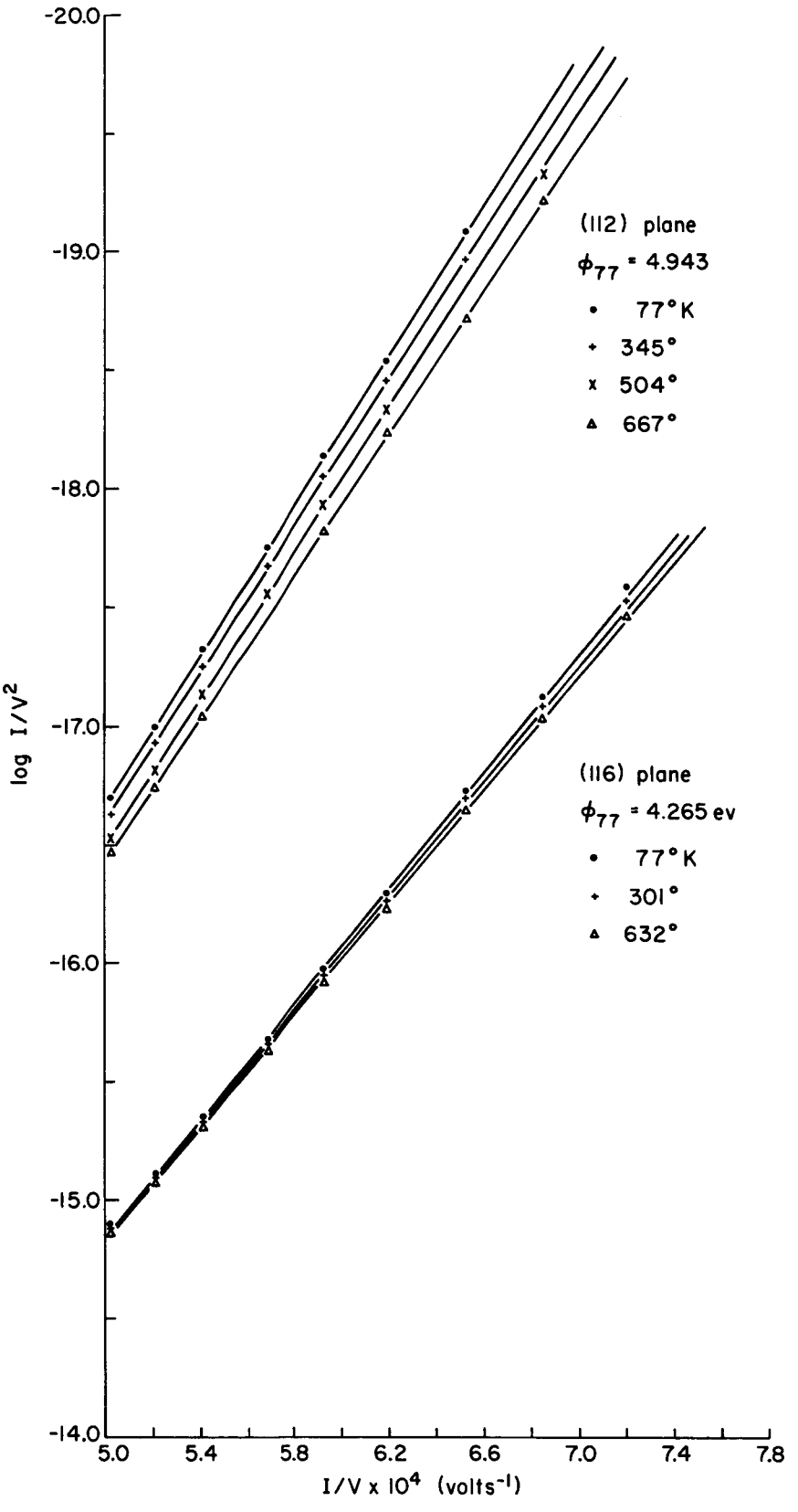

Figure 1. Fowler-Nordheim plots as a function of temperature for two different planes of a tungsten emitter.

factors leading to the resolution limit can be made the latter must suffice as an estimate of the resolution. In our case the emitter axis was along the (100) axis which (as shown later) displayed an anomalous energy distribution shape; therefore, estimate of the best resolution must be obtained from planes off axis using magnetic deflection. Figure 2 shows the current through the electromagnet required to cause deflection along the 110 zone line. Magnetic shielding around the tube reduced the earth's magnetic field to 0, however, the magnetic field in the region of the collector was approximately 0.2 gauss at a beam deflection of 55° (required for (111) measurements). Although no quantitative calculations of the effect of magnetic field on the resolution have been performed, it is believed a field of 0.2 gauss can significantly reduce resolution for this tube design. In the present case resolution for planes off the emitter axis range between 30 - 40mv with poorest resolution at the highest magnet current as expected. Resolution is defined here as the width of the theoretical energy distribution curve at the peak of the experimental curve normalized such that the acceptance potentials and the low energy tails coincide Inasmuch as resolution is not critical except at low temperatures where sharp peaks occur, the resolution at maximum beam deflection was adequate to investigate the energy distribution shapes at elevated temperatures.

THEORY

Total Energy Distribution

In an earlier report the expression for the total energy distribution given was that first obtained by Young and Müller[4] based on a free electron model for the field emitter. Since retarding energy analyzers of the type utilized in this investigation measure total energy distribution (rather than normal energy distribution), it is proper to compare experimental results with expressions for the total energy distribution. It can be readily shown that the total energy of the emitted electrons E collected at a surface of work function ϕ_c must exceed

$$E \geq \phi_c + E_f - V_t \tag{1}$$

where E_f is the Fermi energy and V_t is the bias potential of the emitter. The collected current I_c is related to the total energy distribution $P_t(E)$ as follows:

$$I_c = \int_E^{\infty} P_t(E)\, dE \tag{2}$$

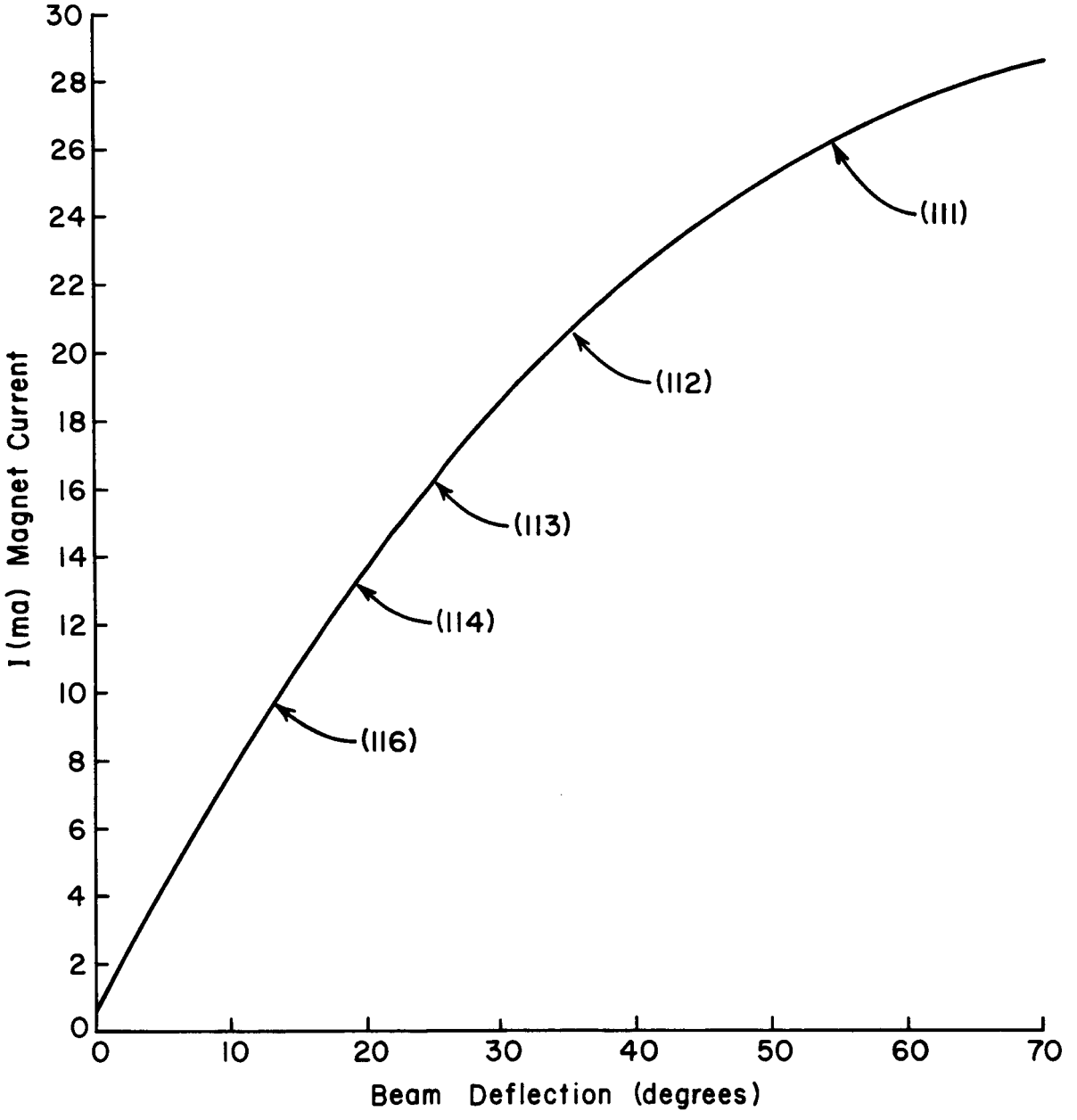

Figure 2. Magnet current I required to deflect beam along the 110 zone of a 001 oriented tungsten emitter.

and

$$P_t(E) = -\frac{dI_c}{dV_t} \tag{3}$$

Thus, $P_t(E)$ can be determined from the gradient of I_c - V_t plots.

Recently, more detailed derivations[5,6] of the energy distribution of field emitted electrons have been given for an arbitrary band structure. It will be instructive to review these derivations, since it is known that the free electron model is not adequate for tungsten[7-10].

The transmission probability for specular transmission (i.e., tangential wave vectors k_y and k_z are conserved) of an electron with energy E_x normal to the barrier depends only on the value of the "x-directed" energy in the barrier region. Transmission coefficient $D(E_{yz}\text{-}E)$ can therefore be written in terms of the transverse k-vector k_{yz}, where

$$E_{yz} = \frac{(hk_{yz})^2}{2m} = \frac{h^2(k^2_y + k^2_z)}{2m} \tag{4}$$

which applies for arbitrary band structures[11].

The total energy distribution is given by

$$P_t(E) = \frac{ef(E)}{2h^3\pi^2}\iint D(k_x)\ dk_y\ dk_z \tag{5}$$

where f(E) is the electron distribution in k-space. Introducing polar coordinates k_{yz} and ϕ_p in the k_y and k_z plane and expressing the maximum value of k_{yz} for a particular polar angle ϕ_p as $k^m_{yz}(E,\phi_p)$ leads to

$$P_t(E) = \frac{ef(E)}{2h^3\pi^2}\int_0^{2\pi}\int_0^{k^m_{yz}} D(k_x)\ d\phi_p\ dk_{yz} \tag{6}$$

where the integral is over all regions of k_{yz} corresponding to positive energy states. Thus, the integration of equation 6 is over the "shadow" of a constant energy surface projected upon a plane perpendicular k_x. The effect of band structure on the distribution can be shown by writing equation 6 in the form

$$P_t(E) = K\frac{f(E)}{2\pi}\left[\int_0^E D(E_x)\,dE_x - \frac{1}{2\pi}\int_0^{2\pi}\int_0^{E-E^m_{yz}} D(E_x)\,d\phi_p dE_x\right] \tag{7}$$

where

$$E_x = E - E_{yz} \quad , \quad E_{yz}^m = \frac{(\hbar k_{yz}^m)^2}{2m} \quad \text{and} \quad \kappa = \frac{4\pi me}{h^3} \tag{8}$$

If $E_{yz}^m(E, \phi_p)$ is sufficiently large (which will be true for Fermi surfaces with large radii of curvature in k-space), the second interval in equation 7 can be neglected and $P_t(E)$ is independent of band structure.

Inserting the first two terms of the WKB approximation

$$D(E_x) = \exp\left[-\beta(E_x)\right] = \exp\left[-b + c(E_x - \epsilon^1)\right] \tag{9}$$

expanded about an arbitrary energy ϵ^1 into equation 7 leads to

$$P_t(E) = \frac{\kappa f(E)\, e^{-b}}{2\pi} \int_0^{2\pi} \int_{E-E_{yz}^m}^{E} e^{c(E_x - \epsilon^1)}\, dE_x d\phi_p \tag{10}$$

provided the quadratic term of the WKB approximation can be neglected and where

$$b = 6.83 \times 10^7\ \phi^{3/2}\, v(y)\ /F \tag{11}$$

$$c = d^{-1} = 10.25 \times 10^7\ \phi^{1/2} t(y)/F \quad (ev^{-1}) \tag{12}$$

with F and ϕ in v/cm and ev respectively.

The integration of equation 10 can be performed by noting that the contribution to the integration comes from values of ϵ^1 near E, so that letting $\epsilon^1 = E$ and integrating yields:

$$P_t(E) = \frac{\kappa f(E)\, e^{-b}}{c} \left[1 - \frac{1}{2\pi} \int_0^{2\pi} e^{-E_{yz}^m/d}\, d\phi_p\right] \tag{13}$$

the second term of equation 13, which manifests band structure effects, is neglible when $E_{yz}^m/d \gg 1$. Normally, d does not exceed a few tenths ev, therefore only those metals exhibiting Fermi surfaces of small radius of curvature (i.e., small positive Fermi energies) are likely to lead to band structure effects perceptable in the total energy distribution results.

In the case of spherical energy surfaces where the effective mass

$m_c = \gamma_c m$ so that $E_{yz}^m = \gamma_c E$, Stratton[5] rewrites Fischer's[6] earlier derived expression of $P_t(E)$ in the form

$$P_t(E) = Kd\, e^{-b} f(E)\, e^{(E-E_f)/d}\left(1-e^{-\gamma_c E/d}\right) \qquad (14)$$

where $E_f > 0$ and the quadratic term of the WKB approximation can be neglected. Again, the term in brackets, which arises from band structure considerations, is of importance only when $(\gamma_c E/d < 1$. Equation 14 reduces to the familiar form first derived by Young[4] when the term in brackets can be neglected. Under these conditions, equation 14 can be expressed in terms of a dimensionless parameter $p = kT/d$ as follows

$$P_t(\epsilon) = \frac{J_o}{d}\left[\frac{e^{\epsilon/d}}{1+e^{\epsilon/pd}}\right] \qquad (15)$$

where $\epsilon = E - E_f$ and the Fermi-Dirac function has been substituted for $f(E)$.

On the basis of equation 14 Stratton[5] also derived the following expression for the energy ϵ_p (relative to the Fermi level) at which the distribution peaks:

$$\frac{\epsilon_p}{kT} = -2.3 \log\left[\frac{1}{p(1+C)} - 1\right] \qquad (16)$$

where

$$C = \gamma_c\left[e^{\gamma_c E_p/d} - 1\right]^{-1} \qquad (17)$$

also, an analytical expression for the half-width $d_{1/2}$ can be obtained at $T=0$ in the form of

$$\frac{d_{1/2}}{d} = 2.3 \log\left[2/\left(1+e^{-E_f/d}\right)\right] . \qquad (18)$$

At $T>0$ values of the half-width must be obtained by numerical or graphical means directly from equation 14.

Work Function Measurements at Elevated Temperature

Measurement of the temperature coefficient of the local work function is possible by analysis of the I_c-V data as a function of temperature according to the Fowler-Nordheim equation. This equation, valid over the range of $0 > p > 2/3$, can be written in the following form:

$$\frac{I_c}{V^2} = \frac{B\pi p}{t(y)\,\phi\,\sin\pi p}\; e^{-b_1 \phi^{3/2} v(y)/\beta(V)} \qquad (19)$$

where B and b_1 are constants and $\beta = F/V$. The instantaneous slope m_a obtained from a "Fowler-Nordheim plot" of $\log I_c/V^2$ vs $1/V$ is

$$m_a = \frac{d\left(\log \frac{I_c}{V^2}\right)}{d\left(\frac{1}{V}\right)} = \frac{V}{2.3}\left(1 - \frac{\pi p}{\tan \pi p}\right) - \frac{b_1 \phi^{3/2} s(y)}{2.3\,\beta} \qquad (20)$$

where $s(y) = 0.951$. At low temperatures (ie, small values of p) the apparent slope becomes

$$m_a \cong \frac{2.83 \times 10^7\, \phi^{3/2}}{\beta} \qquad (21)$$

When the correction term $\Delta = \frac{V}{2.3}(1 - \pi p/\tan \pi p)$ cannot be neglected the temperature dependent work function $\phi(T)$ relative to the low temperature ($77^{\circ}K$) work function ϕ_o is

$$\phi(T) = \phi_o \left(\frac{m_a + \Delta}{m_o}\right)^{2/3} \left(\frac{\beta(T)}{\beta_o}\right)^{2/3} \qquad (22)$$

where $\beta(T)$ allows for thermal expansion of the emitter and is approximately given by

$$\beta(T) = \beta_o \left(1 + \frac{\Delta r}{r}\right) \qquad (23)$$

where $\Delta r/r$ can be obtained from the thermal expansion coefficient of the emitter.

Appropriate values of V and p used in Δ are those midway in the Fowler-Nordheim plot. Within the validity of the Fowler-Nordheim theory the values of $\phi(T)$ determined by equation 22 are rigorous. In practice, excessive curvature in the Fowler-Nordheim plots limits the applicability of such graphical methods to values of $p > 1/2$. However, this limitation is not serious since for clean tungsten, $p = 1/2$ corresponds to an upper temperature limit of $\sim 700^{\circ}K$; furthermore, the onset of surface migration of the emitter and consequent field build-up also sets an upper temperature limit near the latter value.

RESULTS

Total Energy Distribution Measurements

Measurements of the total energy distribution are reported for the (100), (130), (116), (112) and (111) planes of tungsten over the temperature range 77 to 900°K. Care was taken to insure that no change in work function or β due to contamination or field-temperature induced build-up respectively occurred during a given run. Values of I_c ranged from 10^{-9} to 10^{-13} amps depending on the local $\emptyset$ and F. Inasmuch as electronic differentiation was possible only for $I_c \geq 5 \times 10^{-10}$ amps, distribution curves reported herein were obtained from graphical differentiation of x-y recorder plots of I_c vs V_t. From the onset of current collection and position of distribution peaks, particularly at p = 1/2, the position of the Fermi level of the emitter relative to the vacuum level of the collector (ie, $-\emptyset_c = V_t$ according to Equation 1) was set at $V_t = -5.35 \pm 0.05$v.

Typical integral curves from the x-y recorder plots are shown in Figure 3 as a function of temperature. An interesting phenomenon encountered which caused considerable difficulty in obtaining accurate graphical differentiation in the higher temperature (T>500°K) curves of Figure 3 was the onset of flicker noise. Flicker noise, which is proportional to I_c, stems from fluctuations in the local surface potential due to atomic movements at elevated temperatures. Flicker noise was greatly increased by the presence of small amounts of gas contamination and could be used as a criteria of the surface cleanliness. It was also observed that flicker noise was more pronounced at a given temperature on the less densely packed planes of the emitter. It is probably not surprising that flicker noise is rather apparent at such low temperatures, since the tip area "seen" by the 1 mm probe hole on the (100) plane is only 3.0×10^{-14} cm^2 (or approximately 30 atoms) of surface. Thus, at a given temperature 1 atom out of 30 of the surface atoms undergoing place change or movements to metastable positions is probably sufficient to cause detectable flicker noise in the probe current. In order to graphically differentiate integral curves at elevated temperatures smooth curves were drawn through the recorder plotted curves.

A further important feature of the integral curves of Figure 3 is the leveling out of the I_c vs V_t curves at large $-V_t$ and the absence of the well-known[13] decrease in I_c due to reflected primaries at the collector occurring at higher primary energies. Although the important part of the energy distribution curves occurs within 1.5v, it was observed that even at $V_t = -10$v no decrease in I_c occurred; thus, no correction for reflection, which plagued earlier energy analyzers, was necessary for this tube design.

According to equation 15, shapes of energy distribution curves plotted against ϵ/d are a function of only the parameter p. Such theoretical curves

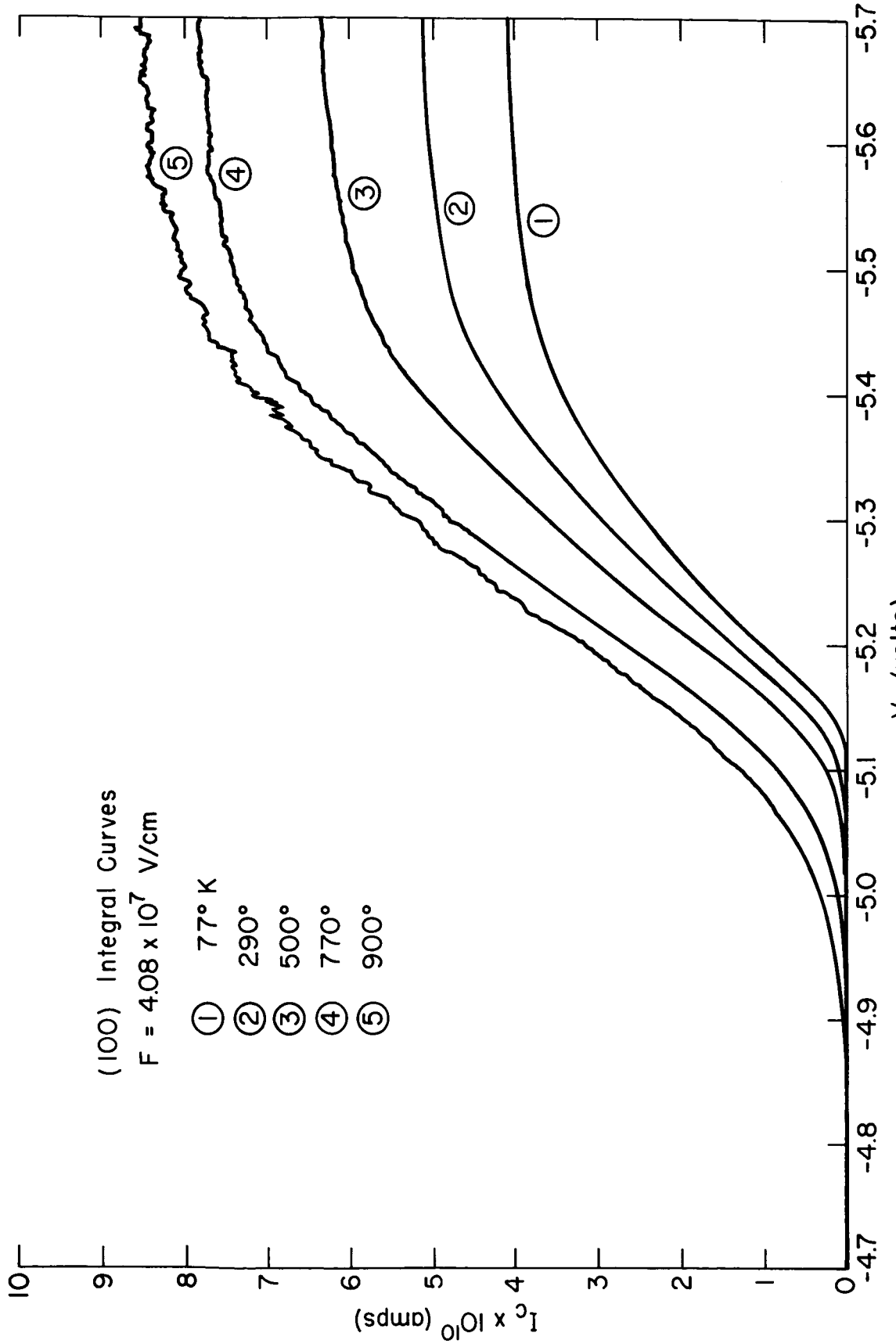

Figure 3. Recorder plots of the probe current I_c as a function of emitter bias voltage V_t at various temperatures.

are shown in Figure 4 for various values of p normalized to give $P_t(\epsilon) = 1$ at $p = \epsilon/d = 0$. The leading edge of the curve at positive ϵ/d stems from the near Boltzman distribution of electrons above the Fermi level at elevated temperatures. Symmetrical energy distribution curves occur at $p = 1/2$ and can be defined in terms of an inversion temperature T^* where

$$T^* = \frac{d}{2k} = \frac{5.67 \times 10^{-5} F}{t(y)\, \phi^{1/2}} \quad (^\circ K) \tag{24}$$

Thus, if charge carriers conduct at or near the Fermi level T^* represents the temperature at which no net energy exchange accompanies field emission. As shown earlier[2] experimental values of T^* are nearly a factor of 2 less than the theoretical predictions of equation 24, thereby indicating either deviations in the energy distribution of the emitted electrons from theory or the occurrence of conduction at levels below the Fermi energy level.

In order to assess whether the energy distribution of the emitted electrons is a cause of the failure of the free-electron model to describe the "Nottingham effect" results, the experimental energy distribution curves are given in Figures 5 through 9. The curves for each plane are given in terms of the parameter p (corresponding to different temperatures in this case) which relates F, ϕ and T in v/cm, ev, and $^\circ K$ as follows:

$$p = 8.82 \times 10^3 \frac{\phi^{1/2} T}{F}\, t(y) \tag{25}$$

Excluding the (100) results, the shapes of the energy distribution curves as a function of p show close similarity to the corresponding theoretical curves of Figure 4. The experimental curves have been normalized vertically such that theoretical and experimental peak heights match near $p = 0.3$. The value of $\epsilon = 0$ (ie, $E_f = -\phi_c = V_t$) was, as mentioned earlier, determined from the position of the leading edge of the low temperature curves and also the point at which the curves cross. The value of $E_f = V_t = -\phi_c = -5.35 \pm 0.05$ ev was used for each curve; this implies a constant ϕ_c over the course of the runs. Thus, small errors in the position of $\epsilon/d = 0$ may occur due to changes in ϕ_c from contamination of the collector.

According to theory the values of $P_t(\epsilon)$ on the trailing edge of the energy distribution curves are nearly coincidental and independent of p. This feature was not confirmed by experiment. For the (112) and (100) distribution curves the values of $P_t(\epsilon)$ along the trailing edge increased with temperature, whereas for the (130), (116) and (111) planes only slight change was observed. Therefore, the energy distribution curve for each plane of Figures 5-9 were multiplied by appropriate factors to cause the trailing

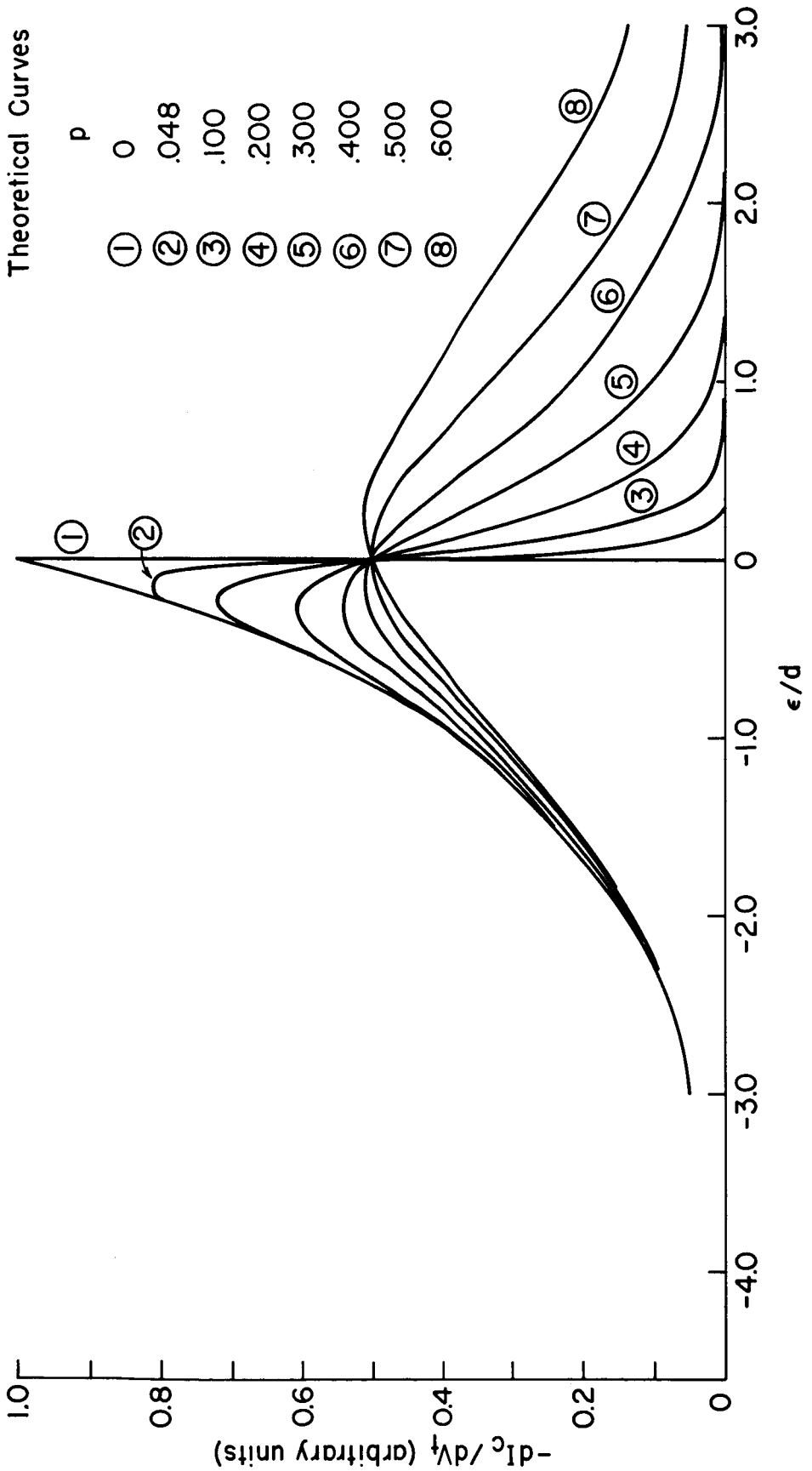

Figure 4. Theoretical total energy distribution plots based on the free electron model (equation 15) at various values of p.

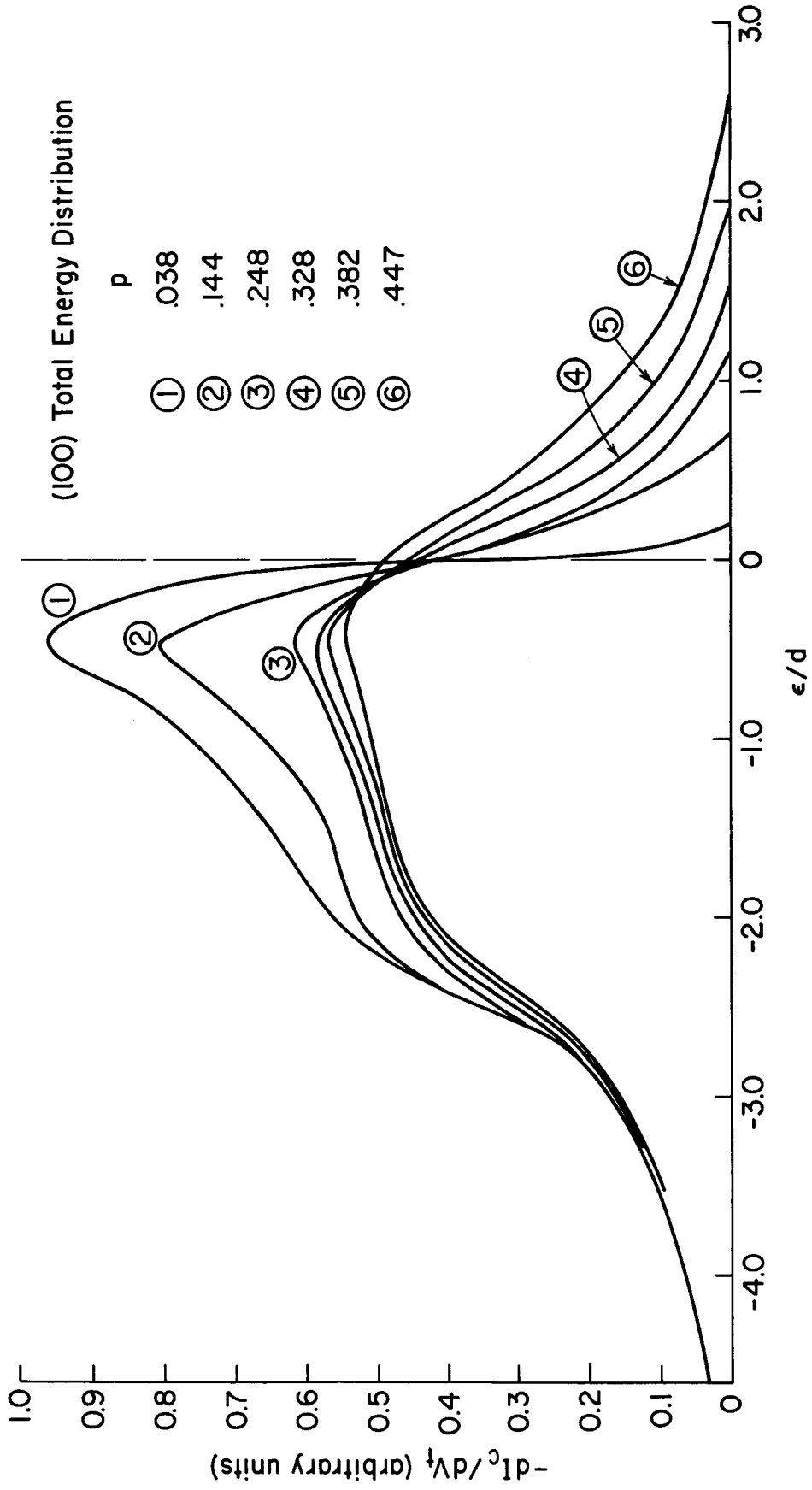

Figure 5. Experimental total energy distribution plots along the [100] direction of a tungsten emitter as a function of p, where d = 0.174 ev and F = 4.08 x 10^7 v/cm.

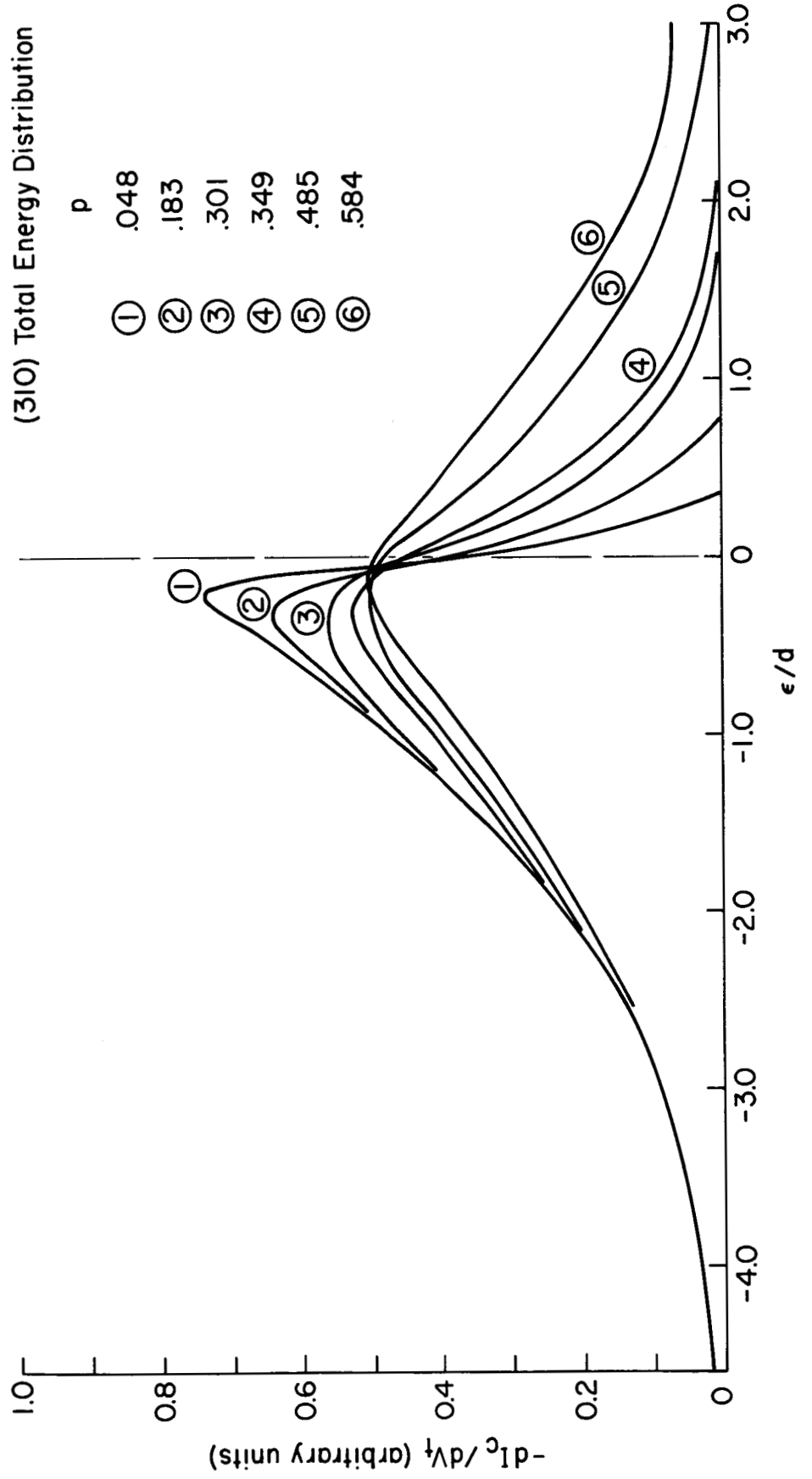

Figure 6. Experimental total energy distribution plots along the [310] direction of a tungsten emitter as a function of p, where d = 0.137 ev and F = 3.06×10^7 v/cm.

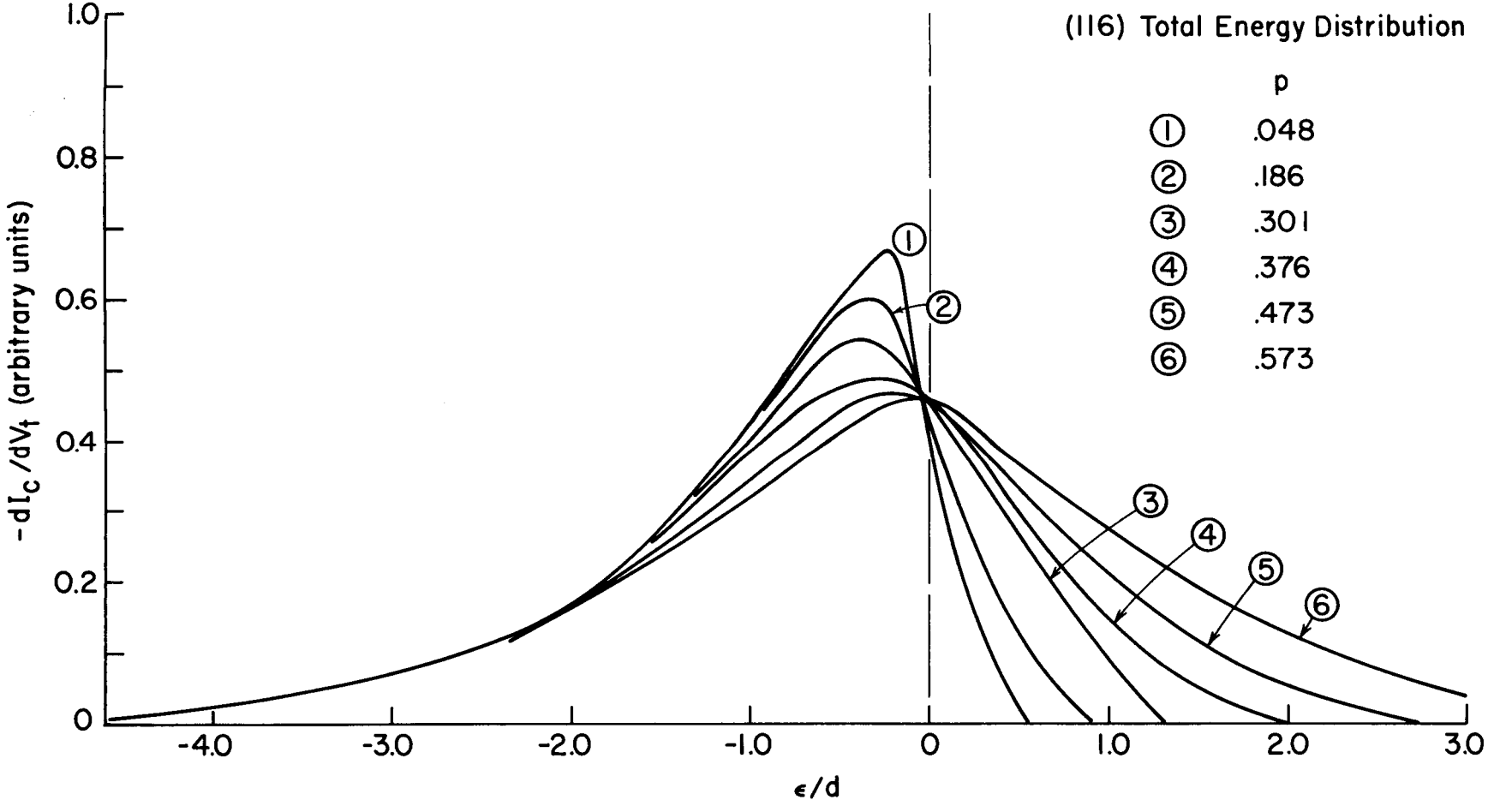

Figure 7. Experimental total energy distribution plots along the [116] direction of a tungsten emitter as a function of p, where d = 0.138 ev and F = 3.04×10^7 v/cm.

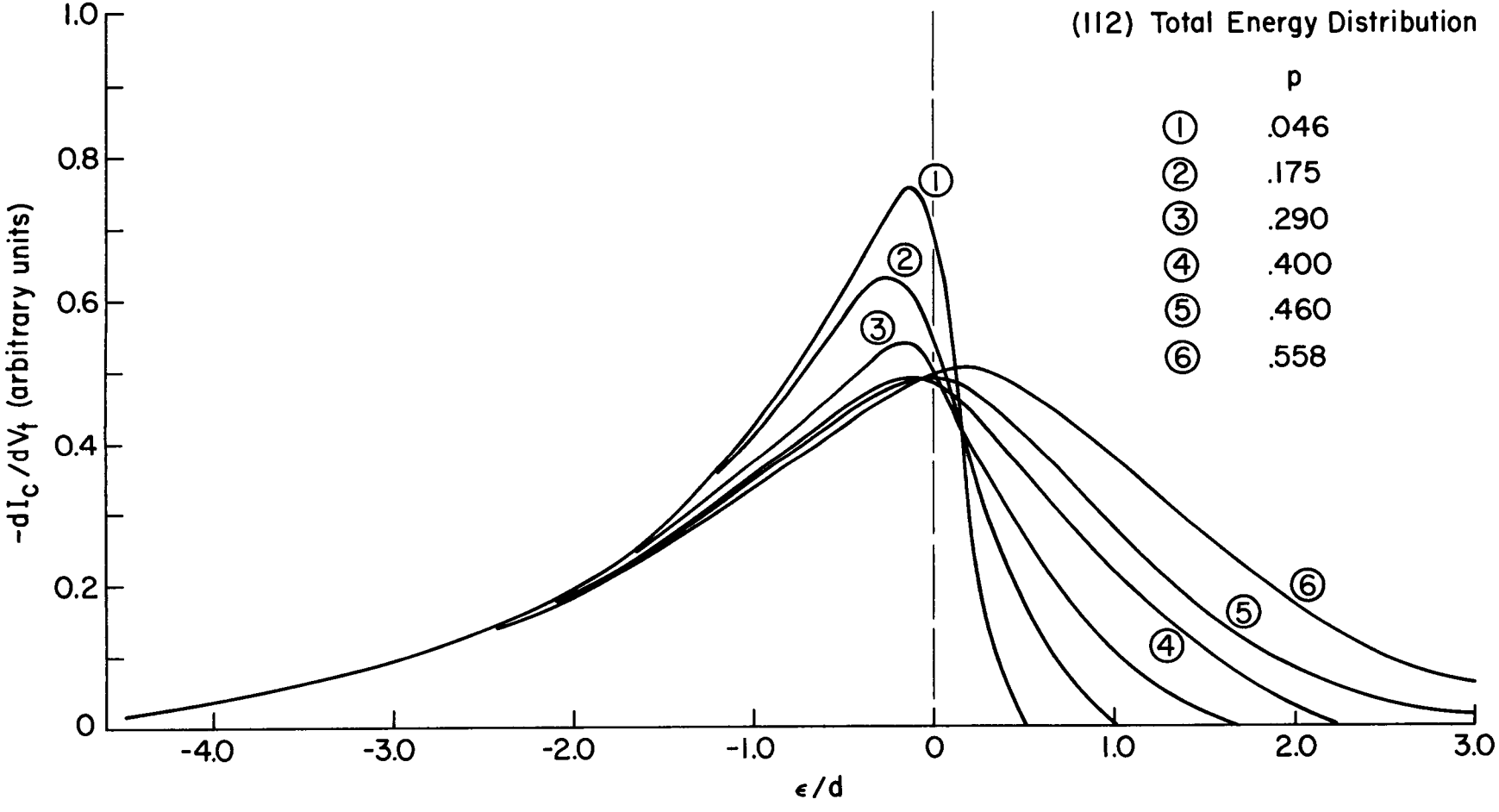

Figure 8. Experimental total energy distribution plots along the [112] direction of a tungsten emitter as a function of p, where d = 0.146 ev and F = 3.48×10^7 v/cm.

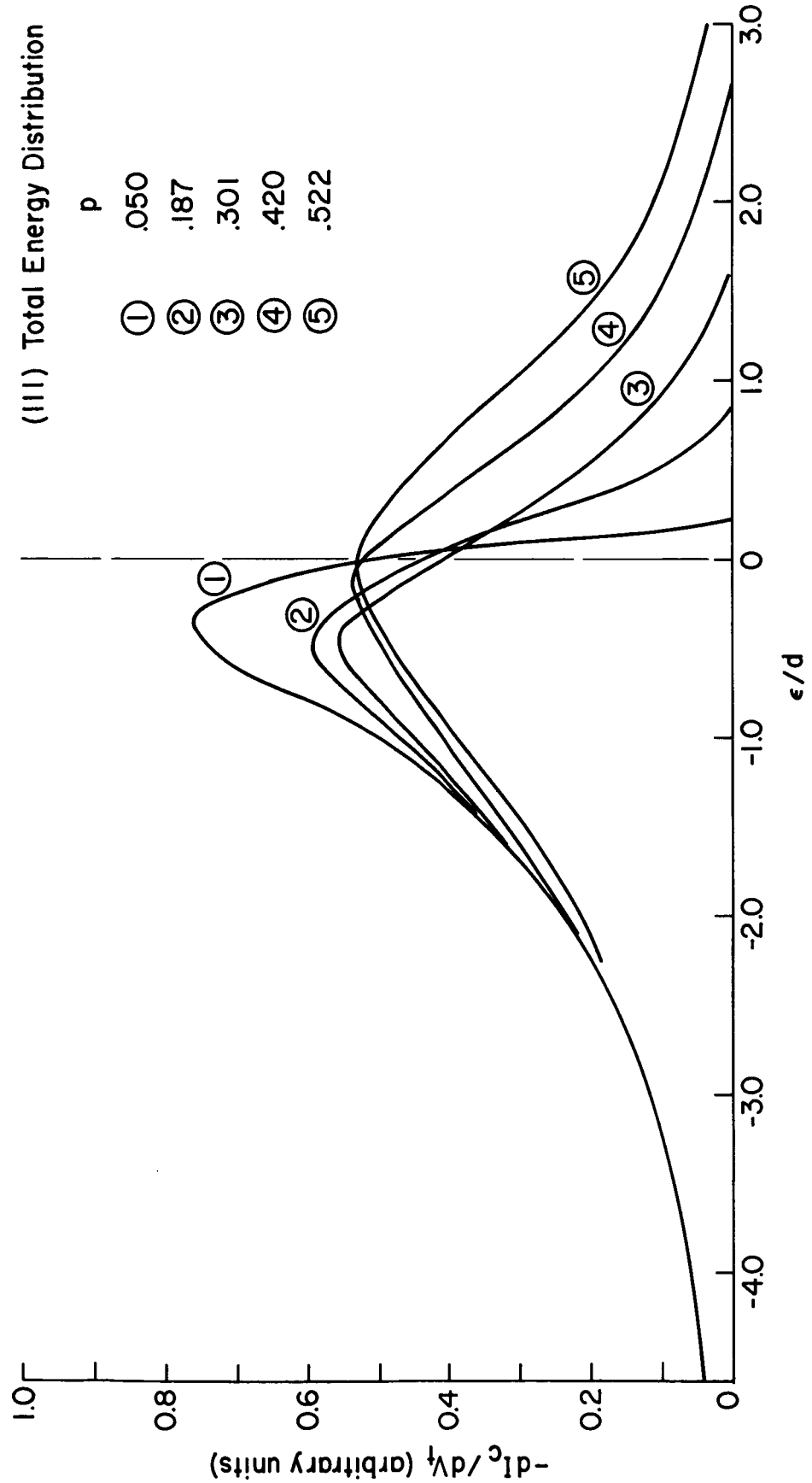

Figure 9. Experimental total energy distribution plots along the [111] direction of a tungsten emitter as a function of p, where d = 0.134 ev and F = 2.99 x 10^7 v/cm.

edges to match at values of $\epsilon/d \leq 2.0$. This was facilitated by plotting the curves on semilog paper. The factors required to cause matching of the trailing edges of the energy distribution curves are given in Table I.

TABLE I

Factors f by which $-dI_c/dV_t$ data were multiplied in order to obtain overlap of low energy portion of curves in Figures 5-9.

(100)		(130)		(116)	(112)		(111)	
p	f	p	f	p f	p	f	p	f
0.038	1	0.048	1.0	f = 1 at	0.046	1.0	0.050	1.0
0.144	0.75	0.183	1.0	all p	0.175	0.83	0.187	0.85
0.248	0.54	0.301	1.0	values	0.290	0.59	0.301	0.79
0.328	0.52	0.349	1.0		0.400	0.52	0.420	0.740
0.382	0.46	0.485	1.35		0.460	6.48	0.522	0.70
0.447	0.435	0.584	1.35		0.558	0.40	0.587	.67

According to equation 15 the relative coherency of the energy distribution curves as a function of p is affected only by variations in d and J_o with p. In the present case where only temperature varies, its affect on J_o and d occurs only through temperature variations of β, the emitting area A and $\emptyset$. Correcting for the apparent change in J_0 and d by using β (T) and A (T) was not sufficient to account for the factors of Table I; therefore, $\emptyset$ (T) variations must be invoked. Calculations showed that both positive (for the (111), (116) and (130)) and negative (for the (110) and (112))temperature coefficients are required to account for the Table I factors. This will be discussed more fully in the next section.

To more fully compare experimental results with theory we have compared the half-widths $d_{1/2}$, the energy distribution peak heights h and the values of ϵ_p at the energy distribution peak with theory in Figures 10-15. The theoretical curves for $d_{1/2}$ and h were obtained graphically from the energy distribution curves of Figure 4. The analytical expression for ϵ_p given in equation 16 was used with C = 0 in Figures 14 and 15.

In view of the strong sensitivity of peak heights and, hence, half-width on the resolution of the analyzer the experimental half-widths are expected to be larger than theory, particularly at low temperatures. Figures 10 and 11 tend to bear out these expectations for all directions except the [100] where significant disagreement with theory is observed. The disagreement of the experimental half-widths with theory for the [100] direction is caused by the anomalous shoulder on the energy distribution curves about 0.35 ev below E_f. We shall now examine the experimental artifacts to which the

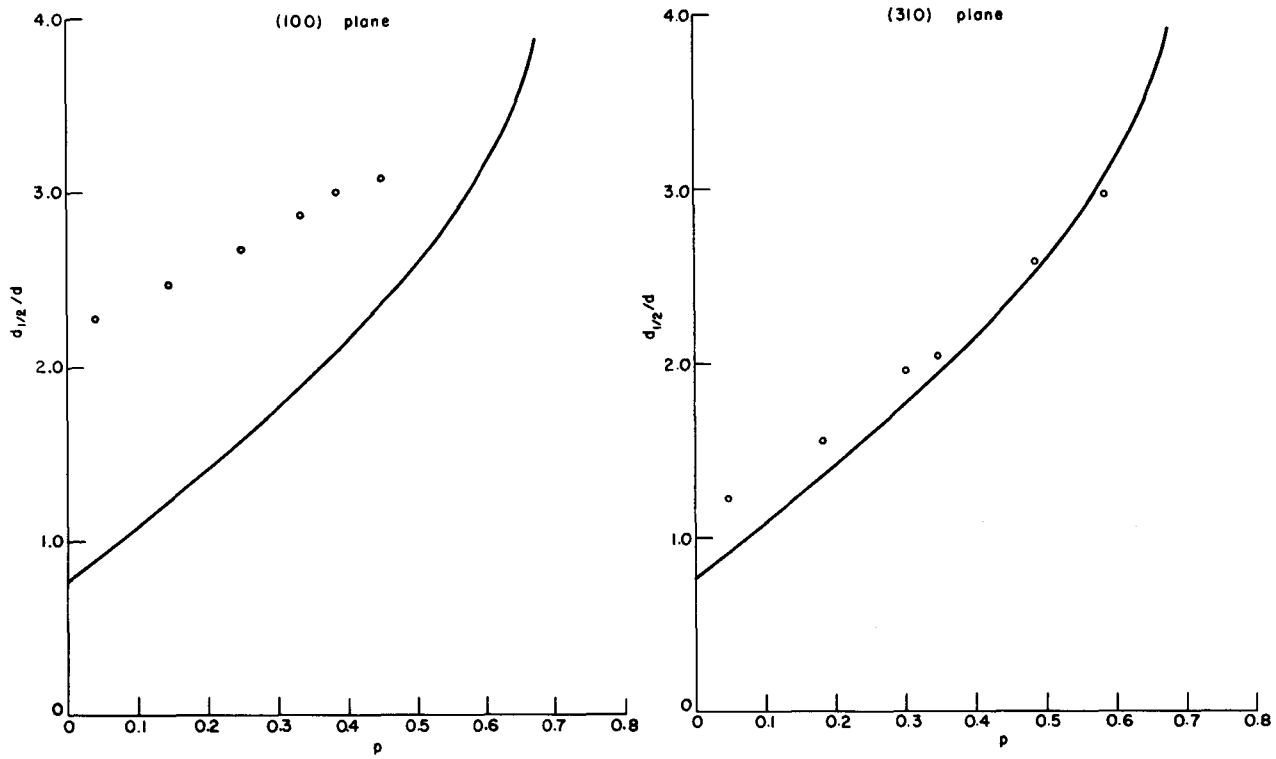

Figure 10. Experimental normalized half-widths d1/2/d of the total energy distribution curves as a function of p. Solid line based on free electron model (equation 15).

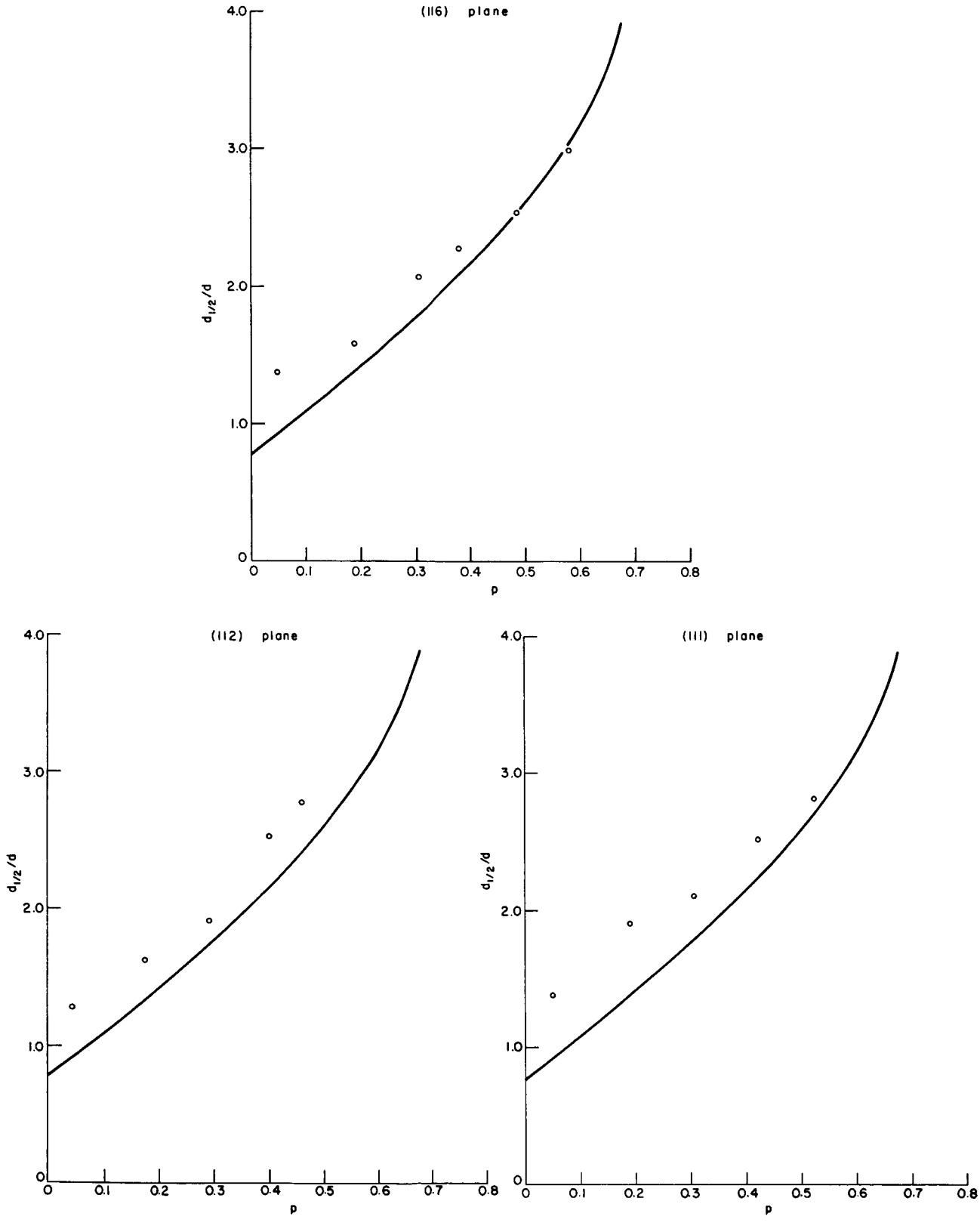

Figure 11. Experimental normalized half-widths of the total energy distribution curves as a function of p. Solid line based on free electron model (equation 15).

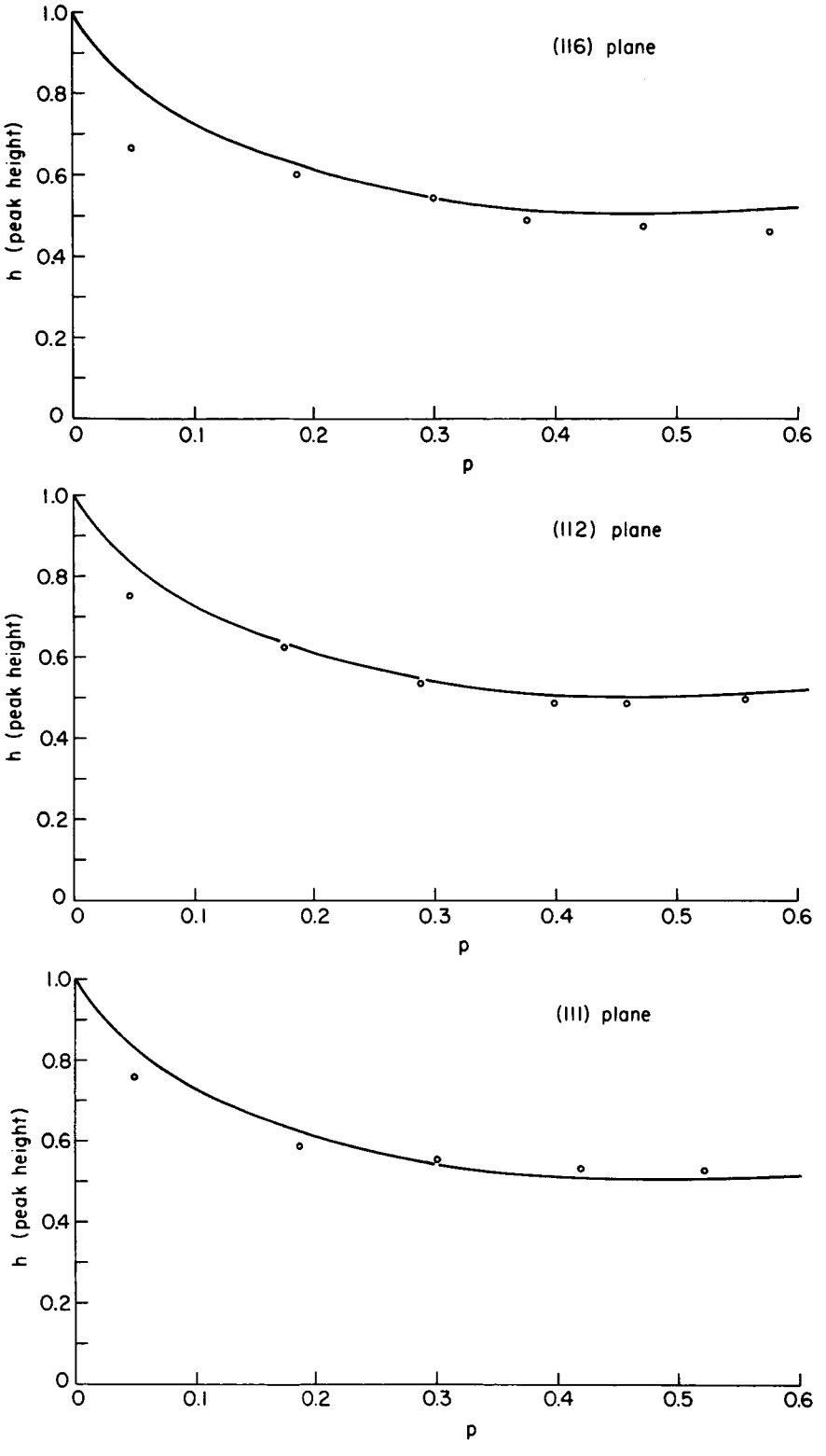

Figure 13. Variation of relative peak height h of the experimental energy distribution curves as a function of p. Solid line based on free electron model (equation 15).

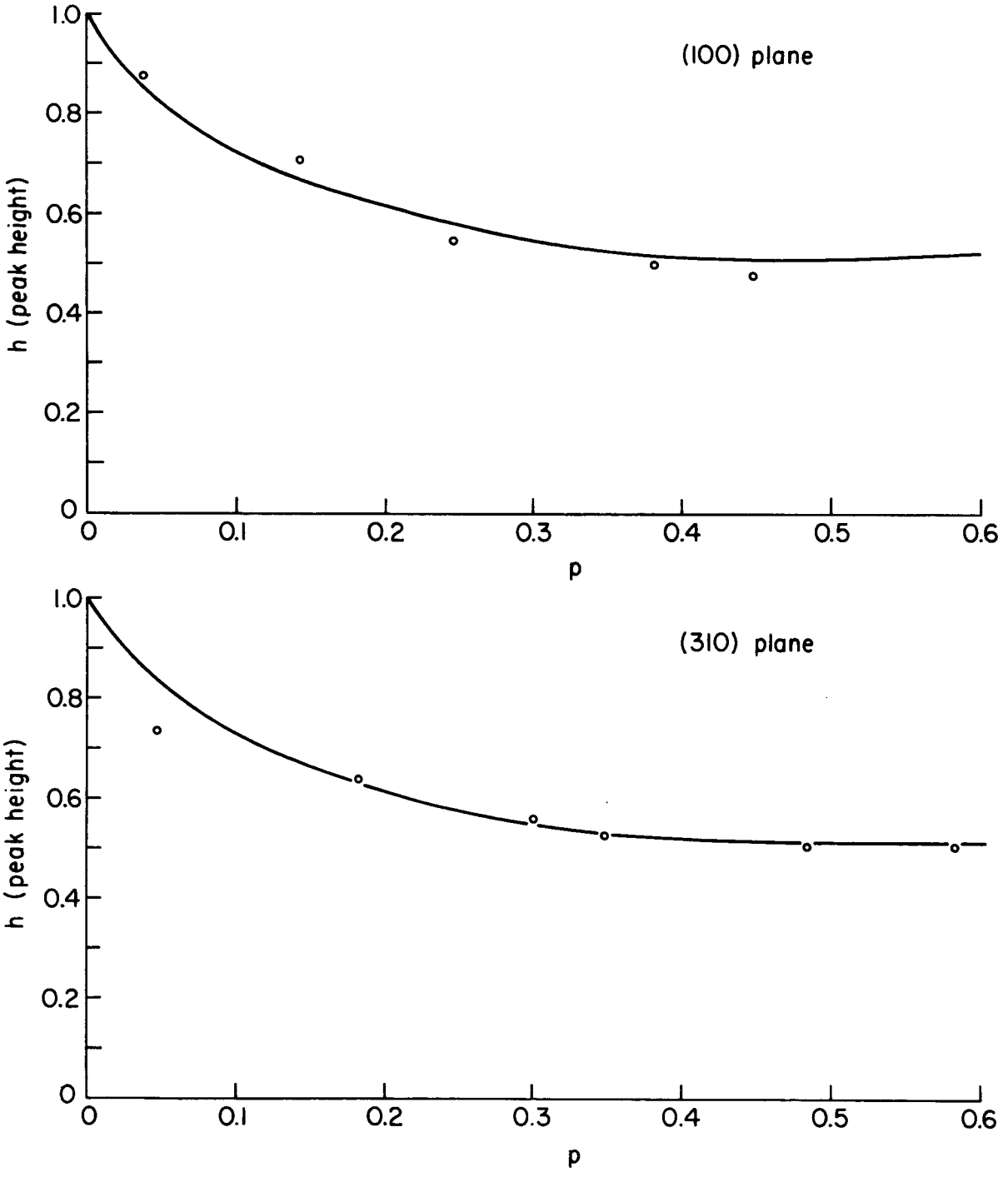

Figure 12. Variation of relative peak height h of the experimental energy distribution curves as a function of p. Solid line based on free electron model (equation 15).

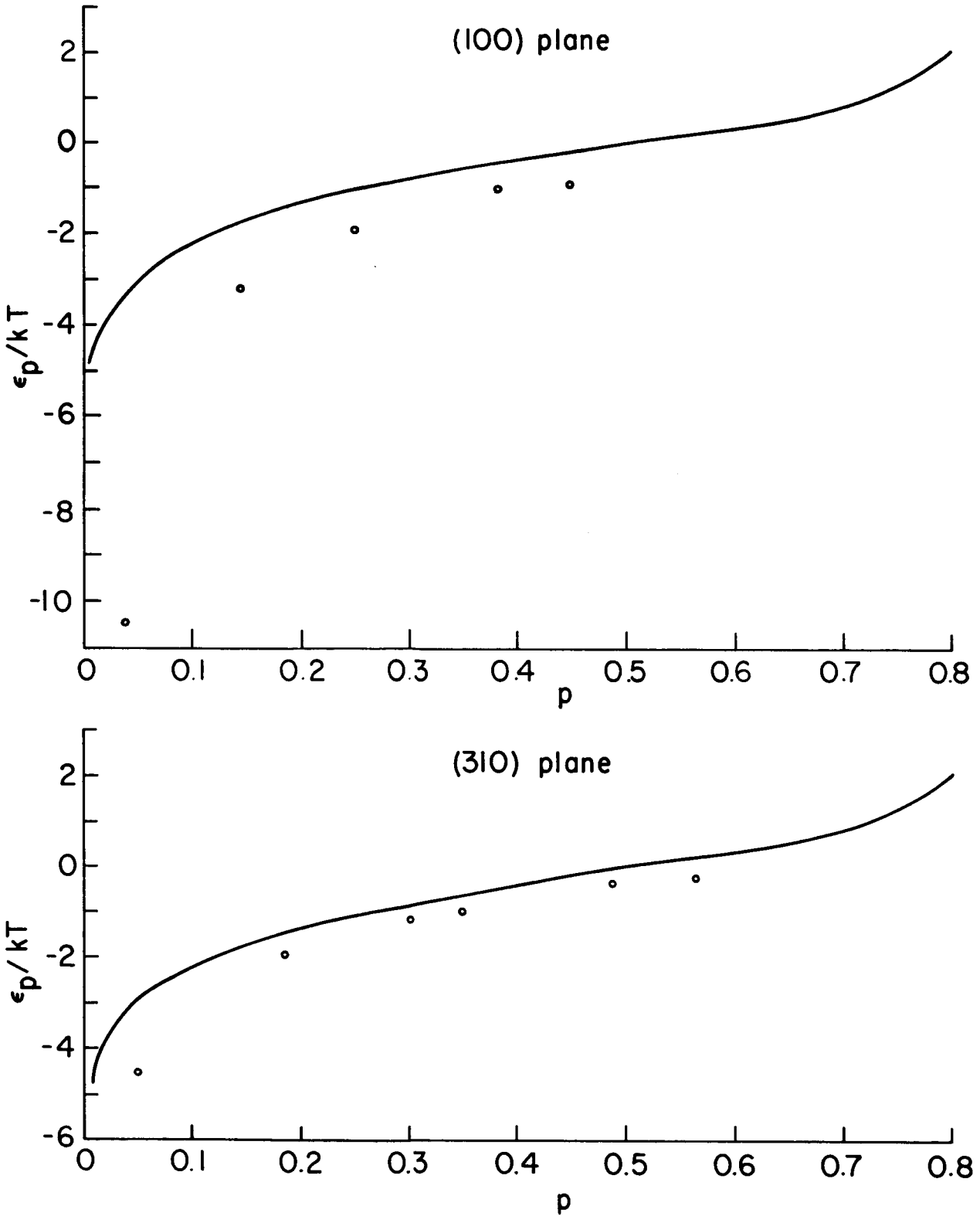

Figure 14. Experimentally observed variation of the position of the energy distribution peak relative to the Fermi level ϵ_p as a function of p. Solid line based on free electron model (equation 15).

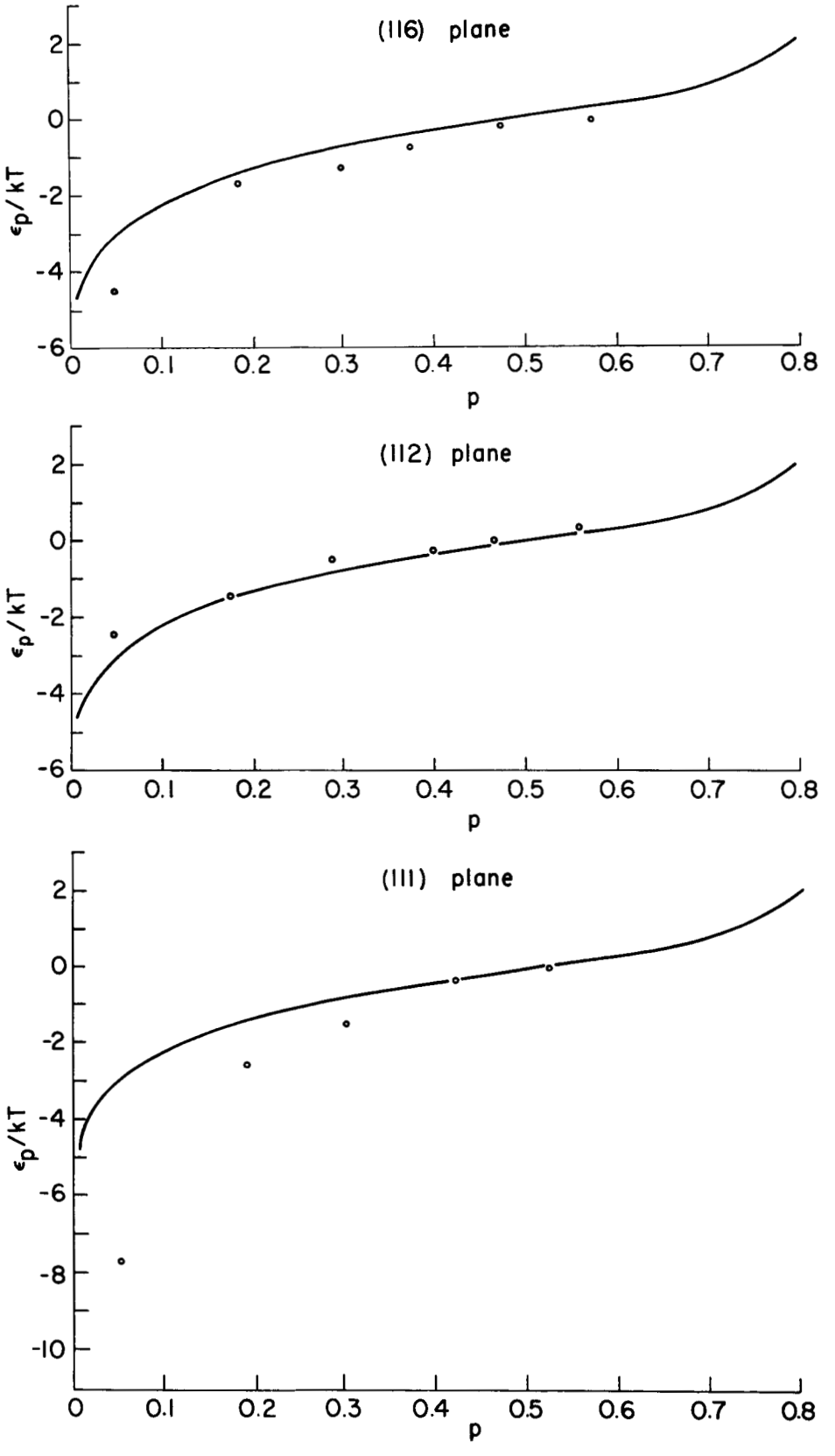

Figure 15. Experimentally observed variation of the position of the energy distribution peak relative to the Fermi level ϵ_p as a function of p. Solid line based on free electron model (equation 15).

shoulder on the (100) energy distribution curves may be attributed.

Two possible explanations for the (100) results are: (1) patch fields at the collector surface and (2) electron optical effects. Patch fields at the collector surface are probably minimized since surface roughness was reduced to less than 1 μ by polishing methods and grain sizes were small compared to the surface area used to collect the electron beam. Furthermore, similar results were obtained on two different collector surfaces. Finally, patch fields should equally affect results from all planes which was not the case. Electron optical effects due to misalignment are not likely since examination of energy distribution curves on identical planes on opposite sides of the [100] direction as much as 54° off tip axis exhibited identical shapes. An emitter with a [130] orientation will be employed in the tube in the near future in order to shed further light on possible electron optical effects leading to the observed (100) results. It is believed, however, on the basis of the above-mentioned results that the observed (100) energy distribution curves are not affected by tube artifacts.

The variation of peak heights h with p in Figures 12 and 13 show good agreement with theoretical expectations except at low values of p where resolution limitations are expected to decrease h values. Surprisingly good agreement even at low p is noted for the (100) results which may be indicative of greater resolution when no magnet current is employed assuming, of course, that the anomalous shoulder does not affect the variation of h with p.

The dependence of the position ϵ_p of the energy distribution peaks relative to E_f shown in Figures 14 and 15 also agrees closely with the free-electron model of tungsten throughout the range of p investigated. Uniform vertical shifts of the experimental points from the theoretical curves shown in (100) and (310) results is attributed to errors in positioning of E_f, caused by variations in ϕ_c.

WORK FUNCTION MEASUREMENTS AT ELEVATED TEMPERATURES

As mentioned in the previous section, it was necessary to multiply values of $P_t(\epsilon)$ for each p by an appropriate factor in order to attain an overlap of curves at $\epsilon/d \lesssim -2$. These factors, given in Table I, suggest a temperature dependent work function with both positive and negative coefficients. To investigate this further, Fowler-Nordheim plots (see Figure 1) as functions of temperature were obtained for the major crystallographic directions. These plots were analyzed according to equation 22 to yield work function values over the temperature range. The change in β due to thermal expansion did not exceed 0.1% and could be neglected. In addition, apparent work function values were corrected for the decrease in β with angle θ from the emitter apex according to the empirical relationship

given by Dyke[14]. The relative values of β for various planes of a [100] oriented emitter are given in Table II. All the work functions and electric fields throughout this report are corrected according to the data of Table II.

Values of work function so obtained and their temperature coefficients are given in Figure 16. In addition, a recent measurement of ϕ (T) for the (110) plane by thermionic methods was reported to yield a temperature coefficient of 14×10^{-5} ev/deg which is interestingly close to the (112) results reported here. The results for tungsten suggests small positive work function temperature coefficients for the low work function planes and larger negative coefficients for the high work function planes.

In summary, the work function temperature coefficient obtained by Fowler-Nordheim plots substantiate the trends of the energy distribution results and show surprisingly large negative coefficients for the (100) and (112) directions.

TABLE II

Decrease in field with angular increase from tip apex θ for [100] oriented emitter (Ref. 14).

θ(deg)	Plane	β/β_o
0	(100)	1.0
13	(113)	0.992
18	(130)	0.985
35	(112)	0.950
45	(110)	0.920
54	(111)	0.890

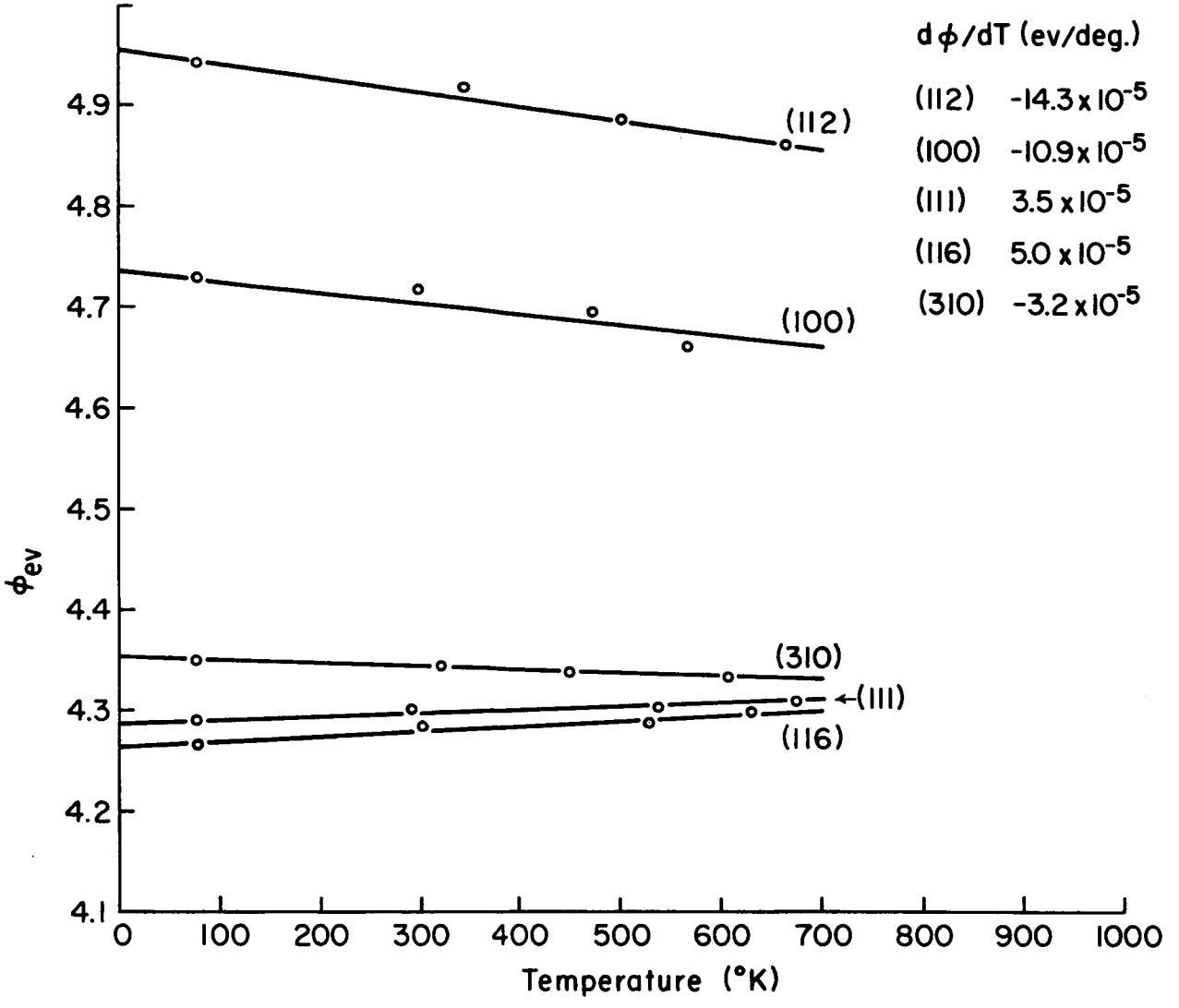

Figure 16. Variation of work function with temperature for the indicated planes as determined by Fowler-Nordheim plots analyzed according to equation 22.

DISCUSSION AND RESULTS

The theoretical considerations of the total energy distribution of field emitted electrons from metals given earlier suggest that, except for Fermi surfaces of small radii of curvature or small m_c/m in the case of spherical surfaces, free-electron theory (ie, equation 15) is adequate. The results reported here generally support this picture for tungsten along the $[11\bar{6}]$, $[11\bar{2}]$, $[111]$ and $[130]$ directions. It should be emphasized, however, that agreement of experimental energy distribution results with equation 15 does not necessarily substantiate the free-electron model for the metal. Agreement with theory basically implies the radius of curvature of the Fermi surface, ie, the maximum value of E_{yz} for a given ϕ_p and E, is sufficiently large to neglect the band structure term of equation 13 along a particular direction. It is interesting to speculate that the shoulder at E_f - 0.35 ev on the energy distribution curve along the $[100]$ direction is due to band structure effects.

Although the exact picture of the Fermi surface for tungsten is not yet established, the salient features, based on other group VI metals can be sketched. According to Lomar[9] band structure of tungsten along the $[100]$, $[111]$ and $[110]$ directions is expected to be similar to that shown in Figure 17 for chromium. The notation of Bouckaert, Smoluchowski and Wigner[16] is employed and Figure 18 shows the Brillouin zone of the body-centered cubic structure with corresponding labeling scheme. The point at which the Fermi level intersects the bands along the various directions defines the Fermi surface in k-space. A two-dimensional extended section of the (100) plane shown in Figure 19 suggests closed electron and hole surfaces centered on Γ and H respectively. In addition, a small pocket of hole and electron surfaces occur at N and along the Γ-H (or $[100]$) direction.

Lomar[9] also suggests extremal diameters along the $[110]$ direction for the Fermi surface and k space as given in Table III. In addition, the ratio of the measured Fermi surface area S to that of a free-electron sphere S_o containing 6 electrons and the number of positive and negative charge carriers, n measured for tungsten are given in Table III[7,8]. In this regards, tungsten is found to be a compensated metal, ie, equal number of negative and positive charge carriers. These results make it clear that the free-electron model is not applicable to describe bulk electron data of tungsten.

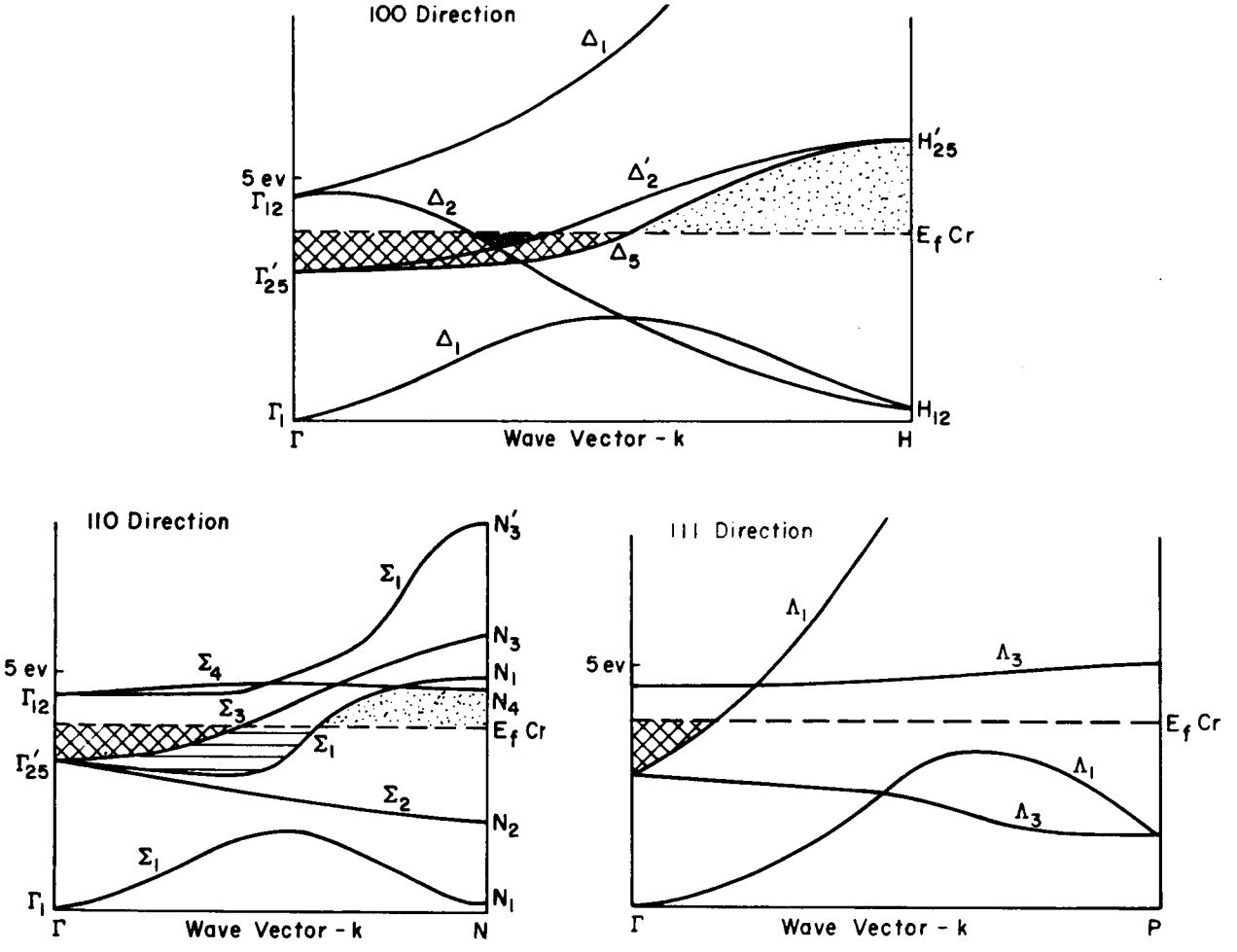

Figure 17. Lomar model of the band structure of chromium (Ref. 9). The other group VI transition metals are probably similar.

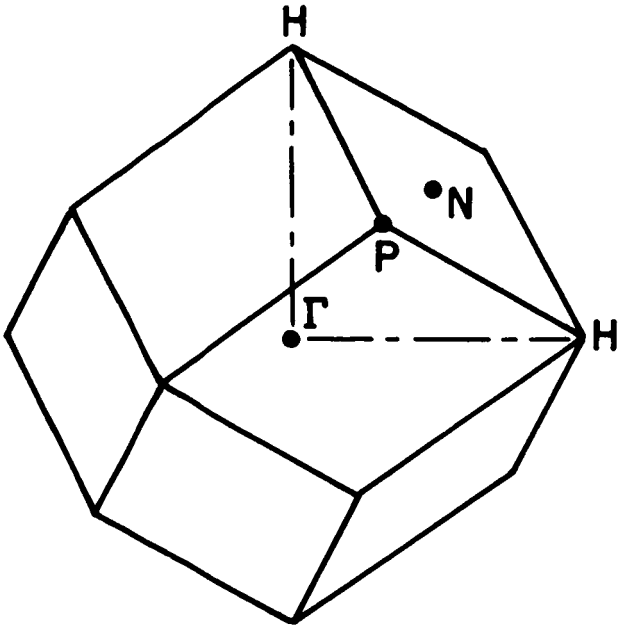

Figure 18. First Brillouin zone of a body-centered cubic structure. Letters indicate directions of reciprocal lattice space used in Figure 17.

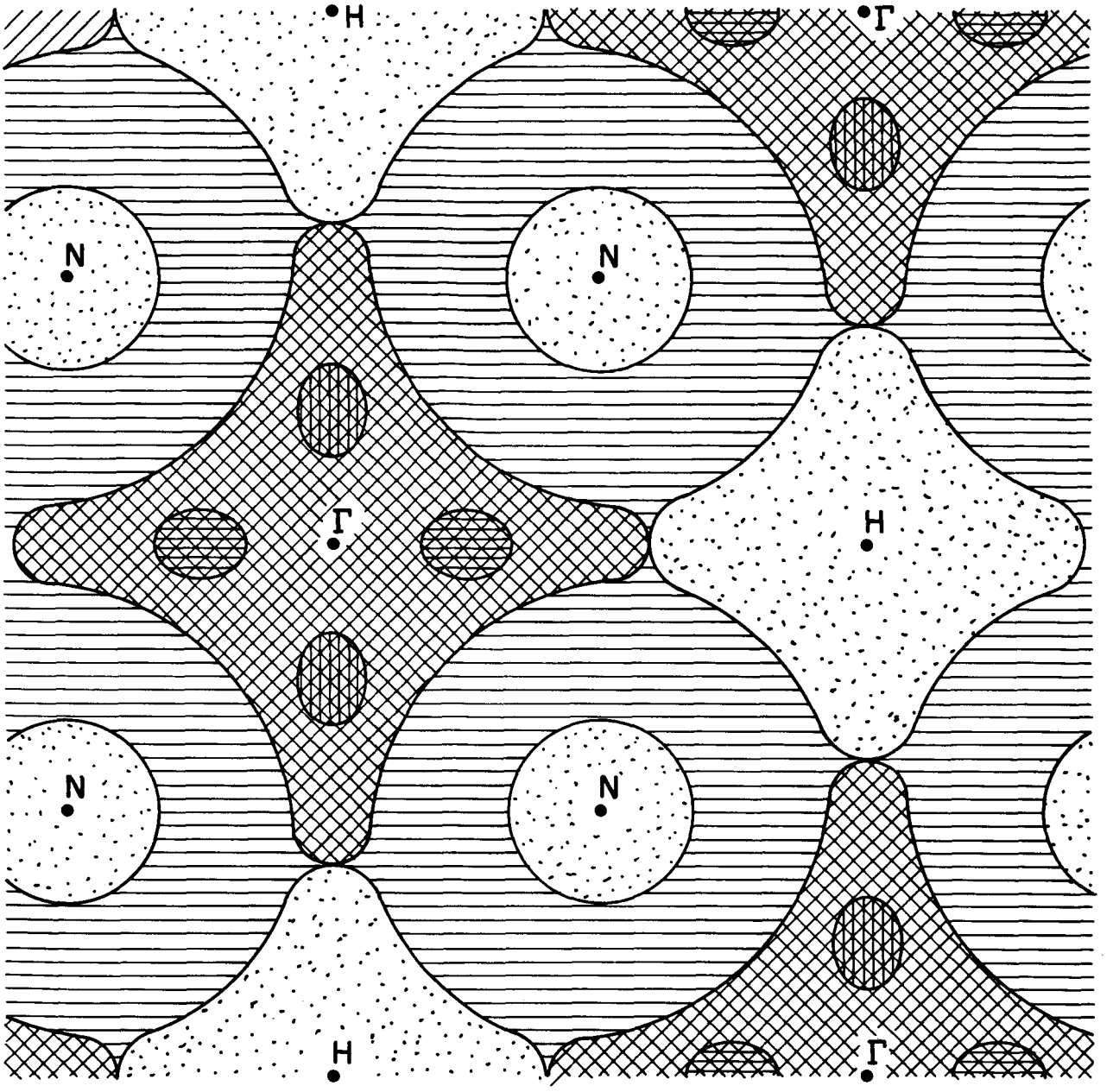

Figure 19. An extended section of the (100) plane in reciprocal lattice space. Each direction of hatching indicates the occupied states in a separate zone, and corresponds to the hatching of Figure 17. The dots indicate hole regions.

TABLE III

Extremal diameters (in reciprocal lattice space) of the Fermi surface along [110] for Tungsten
(where Γ-H$\sim 2 \times 10^{-8}$ cm^{-1})

Electrons at $\Gamma \sim 1 \times 10^{8}$ cm^{-1}

Holes at H $\sim 1.2 \times 10^{8}$ cm^{-1}

Holes at N$\sim 0.4 \times 10^{8}$ cm^{-1}

Electrons on the (100) axis$\sim 0.2 \times 10^{8}$ cm^{-1}

$S/S_o = 0.111$ (Ratio of Fermi surface to free electron sphere containing 6 electrons[7])

n = 0.078 (number of positive and negative charge carriers[7])

The important point to be made from the expected Fermi surface structure is that only the [100] direction has possibilities of perturbing the energy distribution results. This follows from the highly curved Fermi surface and small pocket of electrons along Γ-H of Figure 19 which, according to Figure 17, has a depth of only $\sim .2$ ev below E_f. One is therefore tempted to speculate the shoulder on the experimental energy distribution curves in the [100] directions may be caused by the abrupt termination of the electron pocket along Γ-H a few tenths ev below E_f followed by a shift to energy surfaces with larger E_{yz}^{m} for a given ϕ_p as electrons are emitted from surfaces of lower constant E. The validity of the latter argument awaits further verification of the details of the energy surface at and below the Fermi level.

The appearance of both positive and negative temperature coefficients $d\phi/dT$ for the work function may be interpreted as further evidence of band structure effects. This cannot be stated for certain until all effects leading to a temperature dependent work function are evaluated. These effects have been summarized and given order of magnitude estimates by Herring[17]. Of the several terms contributing to $d\phi/dT$ we shall be interested in those terms which can lead to a $d\phi/dT$ of either sign. According to Herring the effect of electronic specific heat may contribute a term to $d\phi/dT$ of either sign. If the bulk electrons are treated as non-interacting and occupying a continuum of levels of density N(E) per unit energy, the levels being independent of temperature, the standard theory for a degenerate Fermi gas gives

$$E_f = E_f^o - \frac{\pi(kt)^2}{6} \left(\frac{d \ln N(E)}{dE}\right)_{E=E_f^o} + 0\ T^4 - \ldots . \qquad (26)$$

thus

$$\frac{d\phi}{dT} \simeq - \frac{dE_f}{dT} = \frac{(\pi k)^2}{3} T \left(\frac{d \ln N(E)}{dN(E)}\right)_{E=E_f^o} \qquad (27)$$

for free electrons (ie, $N(E) \propto E^{1/2}$),

$$\frac{d\phi}{dT} \simeq \frac{(\pi k)^2}{6} \frac{T}{E_f^o} \qquad (28)$$

which is ordinarily very small. However, for transition metals the existence of narrow, partially filled d bands may greatly alter both the sign and magnitude of N(E) in equation 27. This can be illustrated for a nearly filled band[18] where

$$\frac{d\phi}{dT} \simeq - \frac{(\pi k)^2 T}{6 (E_H - E_f^o)} \qquad (29)$$

and where E_H is the highest energy in the zone. In general, for metals with Fermi levels a few kT from the top or bottom of the band (particularly narrow d-bands) N(E) can be expected to vary considerably from free-electron theory due to differing E-k relationships.

It is interesting to speculate that the negative $d\phi/dT$ values observed along a $[10\bar{0}]$, $[11\bar{2}]$ and $[1\bar{1}0]$ directions may arise from nearly filled narrow d bands along these directions. Examination of the expectant structure of tungsten given in Figure 17 suggests such possibilities exist along the $[1\bar{1}0]$ and $[10\bar{0}]$ directions where nearly filled d bands occur. Further theoretical study of other terms, primarily those arising from lattice expansion, will be needed in order to understand the importance of band structure effects on $d\phi/dT$.

SUMMARY AND CONCLUSIONS

The close agreement of the energy distribution curves with free-electron theory over wide temperature ranges for most crystallographic

directions is probably not a stringent test of the free-electron model in view of the insensitivity of field emitted electrons to specific band structure effects. That the free-electron model is not valid for tungsten is suggested by an anomalous shape in the energy distribution curves in the [100] direction and verified by a variety of solid state measurements. In addition, the occurrence of both positive and negative temperature coefficients along different crystallographic directions can tentatively be attributed to band structure effects. These results strongly suggest that the earlier observed disagreement of the Nottingham effect with theory can be attributed to an enhanced lowering of the charge carrier levels with temperature for the non free-electron tungsten emitter.

REFERENCES

1. L. W. Swanson, et al., Quarterly Report No. 2 for NASA Contract NAS3-5902 (Field Emission Corporation, 1964).

2. L. W. Swanson and L. C. Crouser, Quarterly Report No. 2 for NASA Contract NASw-1082 (Field Emission Corporation, 1965).

3. A. Van Oostrom, PhD Thesis, University of Amsterdam, June, 1965.

4. R. Young, Phys, Rev. 113, 110 (1959).

5. R. Stratton, Phys. Rev. 135, A794 (1964).

6. R. Fischer, Phys, Stat. Sol. 2, 1466 (1962).

7. E. Fawcett and D. Griffiths, J. Phys. Chem Solids 23, 1631 (1962).

8. E. Fawcett, Phys. Rev. 128, 154 (1962).

9. W. Lomar, Proc. Phys. Soc. 80, 489 (1962).

10. E. Fawcett, and W. Reed, Phys. Rev. 134, A723 (1964).

11. W. Harrison, Phys. Rev. 123, 85 (1961).

12. R. Good and E. Müller, Handbuch der Physik 21, 176 (1956).

13. R. Young and E. Müller, Phys. Rev. 113, 115 (1959).

14. W. Dyke, J. Trolan, and W. J. Barnes, J. Appl. Phys. 24, 570 (1953).

15. J. Fine, P. Madey and M. Scheer, Surface Science 3, 227 (1965).

16. L. Bouckaert, R. Smoluchowski, and E. Wigner, Phys. Rev. 50, 58 (1936).

17. C. Herring, Rev. Mod. Phys. 21, 185 (1949).

18. N. Sun and W. Band, Proc. Camb. Phil. Soc. 42, 72, (1946).